ETH

Eidgenössische Technische Hochschule Zürich
Swiss Federal Institute of Technology Zurich

Well-balanced methods for computation of the standing accretion shock instability (SASI)

Master Thesis

Samuel Maloney

January 25, 2019

Advisors: Prof. Dr. Siddhartha Mishra, Dr. Roger Käppeli

Department of Mathematics, Seminar for Applied Mathematics, ETH Zürich

Abstract

Well-balanced schemes are developed for the computation of stationary flows for the Euler equations in the presence of an external potential. The new schemes maintain a discrete equilibrium to machine precision and are applicable across a large class of such equilibria, including both hydrostatic and non-hydrostatic cases. Fundamental to the new method is a local equilibrium reconstruction, using iterative solutions to tie variation in the primitive values to variation in the external potential. The resultant flux and source term discretizations are well-balanced for any choice of consistent numerical flux function. Equations of state beyond the ideal gas law are compatible with the new scheme, which is necessary for many astrophysical problems of interest. Its extension to use on unstructured tetrahedral meshes is also demonstrated, a first for such well-balanced schemes and important for problems involving complex geometry not amenable to structured meshes. Application of the new scheme to a model problem for the standing accretion shock instability is carried out, and evidence for the advective-acoustic cycle—the coupling of vorticity and pressure waves at the shock and as the flow decelerates through a potential step—is observed. The new scheme greatly improves the accuracy of the solutions at the potential step as the underlying equilibrium is precisely maintained throughout the simulation.

i

Contents

Chapter 1

Introduction and Theory

In the study of astrophysical entities, accretion shocks are a fairly commonly encountered physical phenomena. In particular, standing accretion shocks (SAS) are part of the theory behind core-collapse supernovae, with an instability (SASI) described by Blondin et al. [1] being proposed as a possible mechanism for driving the explosive evolution of these physical systems. This instability occurs because of the spherical nature of the system, with the effects of perturbations to the symmetry of the shock being trapped in the interior subsonic region and producing feedback loops which further perturb the shock front.

To gain a better understanding of the underlying mechanisms of this instability, Foglizzo [2] and Sato et al. [3] (hereafter referred to as F09 and SFF09 respectively) proposed and studied a simple toy problem, details of which are presented in Chapter 3. Using this simple set-up they showed evidence for a coupled advective-acoustic cycle between the stationary shock front and an interior decelerating potential step that is intended to model the effects of matter settling onto the surface of the accreting object. This potential step is of particular note in that it gives rise to non-trivial steady state flows which may not be adequately simulated by standard numeric schemes.

For this thesis, therefore, a well-balanced method for simulating steady states in the presence of external potential fields, extended from that developed by Käppeli and Mishra [4] (hereafter referred to as KM14), was applied to the aforementioned toy problem with an eye to higher dimensional simulations of the SASI scenario using circular and spherical geometries. The mathematical theory of fluid flow and associated steady states is briefly outlined in Section 1.1 while an overview of the numerical method and well-balanced scheme used for this thesis is given in Section 1.2. Details of the set-up and results of numerical verification simulations carried out using our implementation of the well-balanced scheme are presented in Chapter 2.

1.1 Euler Equations

The time evolution of the dynamics of fluids can be described by systems of balance laws. For inviscid fluids, this system is given by the well-known Euler equations with source terms, which mathematically represent the physical conservation of mass, momentum, and energy. They are given here following the notation of KM14 as

$$\frac{\partial \rho}{\partial t} + \nabla \cdot (\rho \mathbf{v}) = 0, \tag{1.1a}$$

$$\frac{\partial \rho \mathbf{v}}{\partial t} + \nabla \cdot (\mathbf{v} \rho \mathbf{v}) + \nabla p = -\rho \nabla \phi, \tag{1.1b}$$

$$\frac{\partial E}{\partial t} + \nabla \cdot [(E + p)\mathbf{v}] = -\rho \mathbf{v} \cdot \nabla \phi, \tag{1.1c}$$

where ρ is the mass density, and $\mathbf{v}$ is the local velocity vector. E is the total energy sum of the internal and kinetic energies given as

$$E = \rho e + \frac{\rho v^2}{2}. \tag{1.2}$$

An equation of state $p = p(\rho, e)$ must be selected for a given problem to complete the relations between these primitive quanitites. The quantitiy ϕ on the right-hand side of the latter two equations represents a potential field, such as gravity, which acts upon the fluid. For our purposes, this potential is assumed to be known, either as a given function, through pre-computation, or by solving for it independently of the other fluid quantities at each time step.

The Euler system of equations can be rewritten in the condensed form of a general balance law as

$$\mathbf{U}_t + \nabla \cdot (\mathbf{F}(\mathbf{U})) = \mathbf{S}(\mathbf{U}), \tag{1.3}$$

where $\mathbf{U}$ is a vector of the conserved quantities, and the vectors $\mathbf{F}$ and $\mathbf{S}$ represent the fluxes and sources of these quanitities in the system.

1.1.1 Steady States

For fluid flows in the presence of an external potential field, non-trivial steady states (also called stationary solutions) can arise. Highly accurate simulations of these stationary solutions are of interest as they allow for accurate reproduction and analysis of subsequent perturbations to the system, which can be quite small and therefore overwhelmed by the truncation error of a less well-resolved scheme.

For a steady state solution the time derivative term is exactly zero and it can be seen that the balance law (1.3) reduces to a balance between the fluxes

and sources as

$$\nabla \cdot (\mathbf{F}(\mathbf{U})) = \mathbf{S}(\mathbf{U}). \tag{1.4}$$

In order to find a unique numerical solution to this balance, some constraint on the thermodynamics of the system must be specified. Several options are possible depending on the flow scenario to be modelled, with two important classes comprising constant entropy and constant temperature flows, i.e. isentropic and isothermal flows, respectively. For example, Bernoulli's principle gives us that the following quantity should remain constant along streamlines of an isentropic steady flow

$$\frac{v^2}{2} + \phi + h = \text{constant} \equiv b \tag{1.5}$$

where b is referred to as the Bernoulli constant and h is the specific enthalpy

$$h = e + \frac{p}{\rho}. \tag{1.6}$$

This constancy can then be leveraged in a computational scheme to find the unique weak solution for such an isentropic flow.

1.2 Numerical Methods

It is well-studied that the non-linear nature of the Euler equations (1.1) can lead to very complicated flow features, such as turbulence and shocks, even from initially smooth conditions. As such, numerical solutions to these systems can only be found in a weak sense and require not only initial and boundary conditions, but also additional entropy conditions in order to fix a unique, physically-admissible solution. Many methods have already been developed and well-studied to resolve such flows in a stable and consistent manner, with the class of finite volume methods (FVM) being one of the most popular for conservation laws.

1.2.1 Spatial Discretization

Starting in one dimension for simplicity, the Euler equations in the balance law form (1.3) reduce to

$$\frac{\partial \mathbf{U}}{\partial t} + \frac{\partial \mathbf{F}}{\partial x} = \mathbf{S}, \tag{1.7}$$

where the vectors of conserved quanitities, and their fluxes and sources, are respectively defined as

$$\mathbf{U} = \begin{bmatrix} \rho \\ \rho v_x \\ E \end{bmatrix}, \quad \mathbf{F} = \begin{bmatrix} \rho v_x \\ \rho v_x^2 + p \\ (E + p)v_x \end{bmatrix}, \quad \mathbf{S} = \begin{bmatrix} 0 \\ -\rho \\ -\rho v_x \end{bmatrix} \frac{\partial \phi}{\partial x}. \tag{1.8}$$

3

It is also useful to define a vector of primitive variables $\mathbf{w} = [p,\ v_x,\ T]^T$. While the methods developed here are generally applicable to any choice of the equation of state, the ideal gas law will be assumed as an example for these derivations. It is given by

$$p = \rho e(\gamma - 1), \tag{1.9}$$

where the adiabatic index $\gamma = C_p / C_v$ is the ratio of specific heats at constant pressure and volume, respectively.

A typical FVM discretizes the domain into small cells (i.e. volumes) which in 1D can be denoted $I_i = [x_{i-1/2}, x_{i+1/2}]$ and for simplicity will be assumed to be of uniform size $\Delta x = x_{i+1/2} - x_{i-1/2}$. One then integrates over a given cell I_i and timestep $\Delta t^n = t^{n+1} - t^n$ (also assumed constant) to obtain

$$\mathbf{U}_i^{n+1} = \mathbf{U}_i^n - \frac{\Delta t}{\Delta x} \left(\mathbf{F}_{i+1/2}^n - \mathbf{F}_{i-1/2}^n \right) + \Delta t \mathbf{S}_i^n. \tag{1.10}$$

The ratio of the timestep and grid spacing $\Delta t / \Delta x$ generally must fulfill some CFL condition for stability, and $\mathbf{U}_i^n$ and $\mathbf{U}_i^{n+1}$ are the cell averages of the conserved quantity vectors, which are then evolved in time by computing their fluxes at all of the faces between adjacent volumes.

As the values in these adjacent cells differ in general, a Riemann problem arises at each cell interface, which can then be solved to obtain the fluxes as

$$\mathbf{F}_{i+1/2}^n = \mathcal{F} \left(\mathbf{w}_{i+1/2-}^n, \mathbf{w}_{i+1/2+}^n \right), \tag{1.11}$$

where $\mathbf{w}_{i+1/2-}^n$ and $\mathbf{w}_{i+1/2+}^n$ are the vectors of primitive variables that have been extrapolated from the cell centres at x_i and x_{i+1}, denoted with a trailing '$-$' and '$+$' respectively, to the interface at $x_{i+1/2}$. This means that an FVM requires one to specify this reconstruction scheme to extend the solution values stored as cell average values in order to estimate the values at the cell faces to obtain the Riemann problem at that interface. A piecewise constant reconstruction

$$\mathbf{w}_i^n(x) = \mathbf{w}_i^n, \quad x \in I_i, \tag{1.12}$$

where the cell average value is simply used also at the interface, is the simplest such scheme but gives only first-order accuracy.

Second-order accuracy can be achieved by computing the gradient at each cell centre and using that to linearly extrapolate to the cell faces. However, this method generally gives rise to spurious oscillations in the resulting solutions, particularly near sharp flow features such as shock fronts. To counter this, most such schemes limit the gradient in areas of rapid change, reducing the local order of accuracy towards first-order. These limited schemes are referred to as total variation diminishing (TVD) and various slope limiter

functions, such as those developed by Barth and Jespersen [5], Venkatakrishnan [6, 7], or Michalak and Gooch [8], can be used.

Exact solutions of the flux problems in (1.11) are possible, and are the basis of the so-called Godunov schemes [9], but usually the computational effort is saved by using an approximate solution, such as from a Roe [10], Rusanov [11], or HLLC [12] solver, as the remainder of the method will be itself only approximate due to truncation error. For the following well-balanced schemes, one requires only that the chosen flux function $\mathcal{F}$ be Lipschitz continuous and consistent, i.e. $\mathcal{F}(\mathbf{w}, \mathbf{w}) = \mathbf{F}(\mathbf{w})$, as are the aforementioned examples.

Lastly, up to second-order accuracy the cell average value is equivalent to the value at the cell centre, and so we will treat the two as interchangeable in the following, as only first- and second-order accuracy will be explored.

1.2.2 Well-Balanced Reconstruction

Standard reconstructions as outlined above do not generally preserve equilibrium states exactly, but merely converge towards the precise stationary solution with increasing grid resolution. Particularly for small perturbations, this global error can dominate small features, which then require prohibitively small cell sizes to be adequately resolved. It is therefore desirable to develop a scheme for which the flux and source terms of (1.4) cancel each other exactly for an equilibrium stationary solution. Such a method has been developed for hydrostatic flows by KM14, termed a well-balanced scheme, and the salient results of their derivations are here reproduced and extended to non-hydrostatic equilibria. For simplicity, the concrete case of an isentropic flow will be used here, although it is stressed that the fundamental ideas of the following well-balanced scheme are equally applicable to other thermodynamic conditions.

We will use the thermodynamic definitions of the specific enthalpy (1.6) and specific energy

$$e = \frac{p}{(\gamma - 1)\rho}, \tag{1.13}$$

along with the polytropic form of the equation of state

$$p = p(K, \rho) = K\rho^\gamma, \tag{1.14}$$

where $K = K(s)$ is only a function of the entropy s, and so is constant for isentropic flows. From this, the Bernoulli constant (1.5) can be recast in terms of a single unknown variable, in this case the mass density $\rho(x)$, as

$$\frac{1}{2}\frac{m^2}{\rho^2} + \frac{\gamma}{\gamma - 1}K\rho^{\gamma - 1} + \phi = b, \tag{1.15}$$

where the continuity equation (1.1a) for a steady state shows that the mass flux $m = \rho v_x$ is also constant.

All of the constant values in (1.15) can be computed for a given cell i and timestep n using the stored cell-centred values, and then the the value of $\rho(x)$ throughout the cell can be directly tied to the known variation in $\phi(x)$ as

$$\frac{1}{2} \left(\frac{m_i^n}{\rho_{0,i}^n(x)} \right)^2 + \frac{\gamma}{\gamma - 1} K_i^n \rho_{0,i}^n(x)^{\gamma-1} + \phi(x) = b_i^n. \tag{1.16}$$

This relationship is strongly dependent on the form of the equation of state but is in general non-linear; however, one can compute the value of $\rho_{0,i}^n(x)$ at a specific location by using the iterative Newton-Raphson root-finding algorithm

$$\rho_{0,i,\alpha+1}^n = \rho_{0,i,\alpha}^n - \frac{f(\rho_{0,i,\alpha}^n)}{f'(\rho_{0,i,\alpha}^n)}, \tag{1.17}$$

where $\alpha = 0, 1, 2, \dots$ is simply the iteration number. Specifically, the function $f(\rho_\alpha)$ is given by

$$f(\rho_{0,i,\alpha}^n) = \frac{1}{2} \left(\frac{m_i^n}{\rho_{0,i,\alpha}^n} \right)^2 + \frac{\gamma}{\gamma - 1} K_i^n \left(\rho_{0,i,\alpha}^n \right)^{\gamma-1} + \phi - b_i^n = 0, \tag{1.18}$$

and its derivative $f'(\rho_\alpha)$ as

$$f'(\rho_{0,i,\alpha}^n) = -\frac{(m_i^n)^2}{\left(\rho_{0,i,\alpha}^n \right)^3} + \gamma K_i^n \left(\rho_{0,i,\alpha}^n \right)^{\gamma-2}. \tag{1.19}$$

A stopping criterion $\left| \rho_{0,i,\alpha+1}^n - \rho_{0,i,\alpha}^n \right| < \epsilon$ for some given tolerance ϵ is used to determine convergence of the iterations to a solution for $\rho_{0,i}^n$ of arbitrary accuracy at the desired point, limited only by the machine precision. The computational cost intrinsic to such an iterative solution can be mitigated by using the known cell-centre value as the starting guess $\rho_{\alpha=0}$ which should already be quite close to the final solution at the neighbouring cell interfaces in most instances.

This computaton gives the extrapolated values that $\rho(x)$ would have in the area around the i-th cell for a steady state flow, and so is termed the equilibrium value and denoted with a '0' subscript. If the potential $\phi(x)$ is a known function, then this allows $\rho_0(x)$ to be computed everywhere in the cell neighbourhood; however, if $\phi(x)$ is also given only discretely at the cell centres, perhaps becuase it is itself computed numerically in a separate calculation, then it must be interpolated to the desired reconstruction points (i.e. the cell faces) in order to compute ρ_0 there. A second order accurate piece-wise linear interpolation is generally sufficient, provided the underlying $\phi(x)$ is a continuous function.

Equilibrium reconstruction values for the primitive variables can then be obtained from the computed $\rho_{0,i}^n$, giving

$$\mathbf{w}_{i-1/2+}^n = \begin{bmatrix} p_{0,i}^n(x_{i-1/2}) \\ v_{x,0,i}^n(x_{i-1/2}) \\ T_{0,i}^n(x_{i-1/2}) \end{bmatrix} \quad \text{and} \quad \mathbf{w}_{i+1/2-}^n = \begin{bmatrix} p_{0,i}^n(x_{i+1/2}) \\ v_{x,0,i}^n(x_{i+1/2}) \\ T_{0,i}^n(x_{i+1/2}) \end{bmatrix}, \quad (1.20)$$

as inputs to the chosen Riemann solver at the cell interfaces.

1.2.3 Discretization of Source Terms

To achieve exact balancing of the source and flux terms, we require that the discretizations are not only consistent, but also that the constants and higher order terms of the Taylor expansions precisely match. Following KM14, the definitions used for the source terms are

$$S_{\rho v,i}^n = \frac{\left[\rho_{0,i}^n \left(v_{x,0,i}^n \right)^2 + p_{0,i}^n \right]_{x_{i-1/2}}^{x_{i+1/2}}}{\Delta x} = - \int_{x_{i-1/2}}^{x_{i+1/2}} \rho \frac{\partial \phi}{\partial x} dx + O\left(\Delta x^2 \right), \quad (1.21)$$

$$S_{E,i}^n = -\rho_i^n v_{x,i}^n \frac{\phi_{i+1/2} - \phi_{i-1/2}}{\Delta x} = - \int_{x_{i-1/2}}^{x_{i+1/2}} \rho v_x \frac{\partial \phi}{\partial x} dx + O\left(\Delta x^2 \right), \quad (1.22)$$

where the notation $[f(x)]_a^b \equiv f(x = b) - f(x = a)$ is used for the momentum source term.

Both of these are spatially second-order accurate approximations of the source terms in (1.7), but are specifically chosen such that the higher order error terms will precisely cancel those of the corresponding numerical flux approximations for equilibrium flows. Together these discretizations give the source vector

$$\mathbf{S}_i^n = \begin{bmatrix} 0 \\ S_{\rho v,i}^n \\ S_{E,i}^n \end{bmatrix}. \quad (1.23)$$

Combining the above source vector with the primitives of (1.20) gives a well-balanced scheme which will exactly preserve a given equilibrium state to machine precision, provided the potential is either fully known or defined discretely on the given grid. The scheme will, however, only model perturbations of the equilibrium with first-order accuracy in space.

Proof To prove the well-balancing of the new scheme with these source discretizations, one starts with data that satisfies (1.5) and then inserts it into (1.16) to obtain $\rho_{i+1/2-}^n = \rho_{i+1/2+}^n = \rho_{i+1/2}^n$. From this it can easily be seen that the same must be true for each of the primitive variables,

i.e. $p_{i+1/2-}^n = p_{i+1/2+}^n = p_{i+1/2}^n$ and $v_{x,i+1/2-}^n = v_{x,i+1/2+}^n = v_{x,i+1/2}^n$ and $T_{i+1/2-}^n = T_{i+1/2+}^n = T_{i+1/2}^n$. Using these as inputs to a consistent numerical flux then gives

$$
\begin{aligned}
\mathbf{F}_{i+1/2}^n &= \mathcal{F}\left([p_{i+1/2}^n, v_{x,i+1/2}^n, T_{i+1/2}^n]^T, [p_{i+1/2}^n, v_{x,i+1/2}^n, T_{i+1/2}^n]^T\right) \\
&= \begin{bmatrix} \rho_{i+1/2}^n v_{x,i+1/2}^n \\ \rho_{i+1/2}^n \left(v_{x,i+1/2}^n\right)^2 + p_{i+1/2}^n \\ \left(E_{i+1/2}^n + p_{i+1/2}^n\right) v_{x,i+1/2} \end{bmatrix}.
\end{aligned}
$$

As noted previously, for a flow at equilibrium $m = \rho v_x$ is constant everywhere, so the first entry for the mass flux can simply be replaced by m^n, which is independent of the position. Using this constant m and the relation (1.2) for the total energy, the last entry for the energy flux can be transformed as (dropping the sub- and superscripts briefly for convenience)

$$
\begin{aligned}
(E + p)\, v &= \left(\rho e + \frac{\rho v^2}{2} + p\right) v \\
&= \left(e + \frac{v^2}{2} + \frac{p}{\rho}\right) \rho v \\
&= \left(h + \frac{v^2}{2}\right) m,
\end{aligned}
$$

where the definition (1.6) for the specific enthalpy was used in the final step. Comparing to (1.5) for the Bernoulli constant, the final flux can then be written as

$$
\mathbf{F}_{i+1/2}^n = \begin{bmatrix} m^n \\ \rho_{i+1/2}^n \left(v_{x,i+1/2}^n\right)^2 + p_{i+1/2}^n \\ \left(b^n - \phi_{i+1/2}^n\right) m^n \end{bmatrix}.
$$

Evaluating the source term (1.23) with (1.21) and (1.22) gives

$$
\mathbf{S}_i^n = \frac{1}{\Delta x} \begin{bmatrix} 0 \\ \left[\rho_i^n \left(v_{x,i}^n\right)^2 + p_i^n\right]_{x_{i-1/2}}^{x_{i+1/2}} \\ -\rho_i^n v_{x,i}^n \left(\phi_{i+1/2} - \phi_{i-1/2}\right) \end{bmatrix}.
$$

The expressions for the numerical fluxes and source terms can then be com-

bined to obtain

$$\frac{\mathbf{F}^n_{i+1/2} - \mathbf{F}^n_{i-1/2}}{\Delta x} = \frac{1}{\Delta x} \left[\begin{array}{c} m^n \\ \rho^n_i \left(v^n_{x,i} \right)^2 + p^n_i \\ \left(b^n - \phi^n_i \right) m^n \end{array} \right]^{x_{i+1/2}}_{x_{i-1/2}}$$

$$= \frac{1}{\Delta x} \left[\begin{array}{c} 0 \\ \left[\rho^n_i \left(v^n_{x,i} \right)^2 + p^n_i \right]^{x_{i+1/2}}_{x_{i-1/2}} \\ -\rho^n_i v^n_{x,i} \left(\phi_{i+1/2} - \phi_{i-1/2} \right) \end{array} \right]$$

$$= \mathbf{S}^n_i,$$

which confirms that the flux and source discretizations of the new scheme are well-balanced. $\qquad\square$

### 1.2.4 Extension to Second Order

As first-order accuracy is generally insufficient for most practical problems of interest, the next step is to extend the method to achieve second-order accuracy for perturbations while maintaining the well-balanced properties for the underlying equilibrium. As alluded to at the end of Section 1.2.1, a TVD slope-limited linear extrapolation is used to improve the reconstruction of the primitives to the cell faces. Using 'q' as a placeholder for any of the required primitive variables, we thus define a second-order equilibrium-preserving reconstruction $q_i(x)$ in the i-th cell as

$$q_i(x) = q_{0,i}(x) + Dq_{1,i}(x - x_i), \tag{1.24}$$

where $q_{0,i}(x)$ is the same equilibrium reconstruction computed previously, and $Dq_{1,i}$ is the limited gradient of the perturbation term for the primitive variable within the cell centred at x_i. This perturbation term is denoted by a subscript '1' as $q_{1,i}(x)$ and is given as

$$q_{1,i}(x) = q(x) - q_{0,i}(x). \tag{1.25}$$

It represents the difference between the current solution value $q(x)$ and the purely equilibrium extrapolated values computed for the local cell, and therefore models any perturbations of the flow away from the underlying steady state. Note that when evaluated at the i-th cell centre one will always get $q_{1,i}(x_i) = q_i - q_{0,i}(x_i) = 0$, as the equilibrium reconstruction is computed using the solution values at that cell centre and so will always precisely match the current solution at that location. The illustration in Fig. 1.1 visually shows how the relationship between $p(x)$, $p_{0,i}(x)$, and $p_{1,i}(x)$ might look for a hypothetical pressure curve containing a clearly non-zero deviation from the equilibrium state.
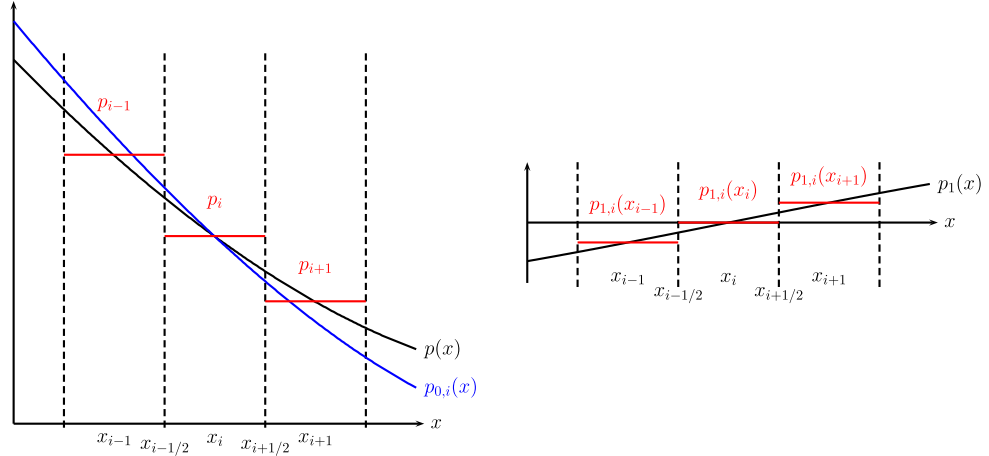
Figure 1.1: This image is taken directly from KM14 [4]. In the left pane, the reconstruction begins with only the cell average values, shown in red, which to second-order accuracy are equal to the current solution $p(x)$, shown in black, evaluated at the cell centres. The blue line shows the value of the equilibrium $p_{0,i}(x)$ extrapolated from the constant values computed at the i-th cell centre. Subtracting the blue line from the black line then gives the perturbation function $p_{1,i}(x)$ in the right pane.

Because the current solution $q(x)$ is known only at the cell centres, the required local slope is determined by computing the value of $q_{0,i}(x)$ not only at the cell faces as in the first-order case, but also at the neighbouring cell centres. These extrapolated values are then subtracted from the known solution values at those cell centres as

$$q_{1,i}(x_{i-1}) = q_{i-1} - q_{0,i}(x_{i-1}) \quad \text{and} \quad q_{1,i}(x_{i+1}) = q_{i+1} - q_{0,i}(x_{i+1}). \quad (1.26)$$

The limited slope can then be computed by applying a TVD limiter function to the estimates of the local slope obtained from the neighbouring perturbation values as

$$Dq_{1,i} = \text{limiter}\left(\frac{q_{1,i}(x_i) - q_{1,i}(x_{i-1})}{\Delta x}, \frac{q_{1,i}(x_{i+1}) - q_{1,i}(x_i)}{\Delta x}\right). \quad (1.27)$$

There are many potential choices of limiter function described in the literature, one of the most common and simple of which is the *minmod* limiter, defined as

$$\text{minmod}(a, b) = \frac{1}{2}\left(\text{sign}(a) + \text{sign}(b)\right)\min\left(|a|, |b|\right). \quad (1.28)$$

As noted earlier, the perturbation terms will be zero at the current cell centre, and so the final form of the second-order reconstruction simplifies to

$$q_i(x) = q_{0,i}(x) + \text{limiter}\left(-\frac{q_{1,i}(x_{i-1})}{\Delta x}, \frac{q_{1,i}(x_{i+1})}{\Delta x}\right)(x - x_i). \quad (1.29)$$

It is easy to see that for a flow which is already at equilibrium, the equilibrium reconstruction $q_{0,i}(x)$ will be precisely equal to the solution values $q(x)$ at the neighbouring cells, and so the $q_{1,i}(x)$ terms in (1.29) will all be zero by design. Thus, for already steady state flows it reduces to the first-order scheme previously derived, thereby preserving the equilibrium exactly also for this second-order scheme. The final vectors of primitive values which are input to the Riemann solver are

$$
\mathbf{w}^n_{i-1/2+} = \begin{bmatrix} p^n_{0,i}(x_{i-1/2}) + p^n_{1,i}(x_{i-1/2}) \\ v^n_{x,0,i}(x_{i-1/2}) + v^n_{x,1,i}(x_{i-1/2}) \\ T^n_{0,i}(x_{i-1/2}) + T^n_{1,i}(x_{i-1/2}) \end{bmatrix}
$$

and   (1.30)

$$
\mathbf{w}^n_{i+1/2-} = \begin{bmatrix} p^n_{0,i}(x_{i+1/2}) + p^n_{1,i}(x_{i+1/2}) \\ v^n_{x,0,i}(x_{i+1/2}) + v^n_{x,1,i}(x_{i+1/2}) \\ T^n_{0,i}(x_{i+1/2}) + T^n_{1,i}(x_{i+1/2}) \end{bmatrix} .
$$

The same discretization of the source terms as in (1.21) and (1.22) are used, as they are already second-order accurate and must remain unchanged to preserve the well-balanced property of the reconstruction for equilibrium flows.

1.2.5   Time Discretization

After specifying a spatial discretization, the system of equations (1.3) can be written in the semi-discrete form

$$
\mathbf{U}_t = \mathbf{R}(\mathbf{U}),
\tag{1.31}
$$

where $\mathbf{R}$ is a simple notation to represent the residual from the chosen spatial scheme, as outlined above.

The time discretization which is then used to advance the solution is a four-stage, low-storage Runge-Kutta (RK) scheme with the following form

$$
\begin{aligned}
\mathbf{U}^{(0)} &\equiv \mathbf{U}^n, \\
\mathbf{U}^{(i)} &= \mathbf{U}^{(0)} + \beta_i \Delta t \mathbf{R}\left(\mathbf{U}^{(i-1)}\right), \qquad i = 1,2,3,4, \\
\mathbf{U}^{n+1} &\equiv \mathbf{U}^{(4)},
\end{aligned}
\tag{1.32}
$$

where n is the global time index, i is the index of the intra-timestep RK stage, and $\Delta t = t^{n+1} - t^n$ is the size of the current time step. The specific time-marching scheme used is described in [13] and has the coefficients

$$
\beta_1 = 0.11, \quad \beta_2 = 0.2766, \quad \beta_3 = 0.5, \quad \beta_4 = 1.
\tag{1.33}
$$

Having $\beta_4 = 1$ ensures that such a scheme is consistent, and having $\beta_3 = 0.5$ means the method is second-order accurate for both linear and non-linear

equations. The values for β_1 and β_2 were designed to maximize the largest stable CFL coefficient, and therefore possible timestep size, when paired with upwind based spatial discretization schemes. According to [14] and [15], having every $\beta_i \geq 0$ also means that the scheme belongs to the desirable class of strong stability preserving (SSP) RK methods.

1.2.6 Multiple Spatial Dimensions

Extending the method to multiple spatial dimensions is accomplished via a relatively straightforward application of the preceding 1D approach along each additional dimension. It is summarized here for 2D but would progress analgously for 3D cases.

The 1D Euler equation (1.7) is expanded to 2D as

$$\frac{\partial \mathbf{U}}{\partial t} + \frac{\partial \mathbf{F}}{\partial x} + \frac{\partial \mathbf{G}}{\partial y} = \mathbf{S}, \tag{1.34}$$

where the conserved quantities, fluxes, and source terms are now given by the four-valued vectors

$$\mathbf{U} = \begin{bmatrix} \rho \\ \rho v_x \\ \rho v_y \\ E \end{bmatrix}, \quad \mathbf{F} = \begin{bmatrix} \rho v_x \\ \rho v_x^2 + p \\ \rho v_x v_y \\ (E+p)v_x \end{bmatrix}, \quad \mathbf{G} = \begin{bmatrix} \rho v_y \\ \rho v_x v_y \\ \rho v_y^2 + p \\ (E+p)v_y \end{bmatrix},$$

$$\mathbf{S} = \mathbf{S}_x + \mathbf{S}_y = \begin{bmatrix} 0 \\ -\rho \\ 0 \\ -\rho v_x \end{bmatrix} \frac{\partial \phi}{\partial x} + \begin{bmatrix} 0 \\ 0 \\ -\rho \\ -\rho v_y \end{bmatrix} \frac{\partial \phi}{\partial y}, \tag{1.35}$$

and $\mathbf{w} = [p, \ v_x, \ v_y, \ T]^T$ is the vector of primitive values.

Analgously to the 1D case, one starts by computing the equilibrium constants b_i^n, K_i^n, and m_i^n at the cell centres and using those to extrapolate the local subcell equilibrium to the cell faces based on the changes in the potential $\phi(x,y)$ from the cell centres to the faces. If $\phi(x,y)$ is known only discretely, then a bilinear interpolation will now be needed to determine its value at the cell faces. The first-order primitive vector of inputs to the Riemann solver are then

$$\mathbf{w}_{i\mp1/2\pm,j}^n = \begin{bmatrix} p_{0,i,j}^n(x_{i\mp1/2}, y_j) \\ v_{x,0,i,j}^n(x_{i\mp1/2}, y_j) \\ v_{y,0,i,j}^n(x_{i\mp1/2}, y_j) \\ T_{0,i,j}^n(x_{i\mp1/2}, y_j) \end{bmatrix}, \quad \mathbf{w}_{i,j\mp1/2\pm}^n = \begin{bmatrix} p_{0,i,j}^n(x_i, y_{j\mp1/2}) \\ v_{x,0,i,j}^n(x_i, y_{j\mp1/2}) \\ v_{y,0,,ji}^n(x_i, y_{j\mp1/2}) \\ T_{0,i,j}^n(x_i, y_{j\mp1/2}) \end{bmatrix}. \tag{1.36}$$

The source terms can now be split into a sum of components from the individual dimensions, which are then individually specified similarly as in the

1D case, giving

$$\mathbf{S}_{i,j} = \mathbf{S}_{x,i,j} + \mathbf{S}_{y,i,j} = \begin{bmatrix} 0 \\ S_{x,\rho v,i,j} \\ 0 \\ S_{x,E,i,j} \end{bmatrix} + \begin{bmatrix} 0 \\ 0 \\ S_{y,\rho v,i,j} \\ S_{y,E,i,j} \end{bmatrix}, \tag{1.37}$$

where the momentum source terms are given by

$$\begin{aligned}
S_{x,\rho v,i,j} &= \frac{\left[\rho_{0,i,j}^n (v_{0,i,j}^n)^2 + p_{0,i,j}^n \right]_{x_{i-1/2}}^{x_{i+1/2}}}{\Delta x} \quad \text{and} \\
S_{y,\rho v,i,j} &= \frac{\left[\rho_{0,i,j}^n (v_{0,i,j}^n)^2 + p_{0,i,j}^n \right]_{y_{j-1/2}}^{y_{j+1/2}}}{\Delta y},
\end{aligned} \tag{1.38}$$

and the energy source terms are given by

$$S_{x,E,i,j}^n = -\rho v_{x,i,j}^n \frac{\phi_{i+1,j} - \phi_{i-1,j}}{2\Delta x} \quad \text{and} \quad S_{y,E,i,j}^n = -\rho v_{y,i,j}^n \frac{\phi_{i,j+1} - \phi_{i,j-1}}{2\Delta y}. \tag{1.39}$$

These source discretizations are again second-order accurate as in the 1D case, and combined with (1.36) they give a scheme which is precisely equilibrium preserving but only first-order accurate for modelling deviations from the steady state.

This can then be improved to second-order by proceeding dimension-by-dimension as in the 1D case and computing the differences between the local equilibrium reconstruction evaluated at the neighbouring cell centres and the solution values there, to create a local subcell reconstruction of the perturbations using a gradient-limited linear approximation. This leads to the following second-order accurate primitve vectors

$$\begin{aligned}
\mathbf{w}_{i\mp 1/2\pm,j}^n &= \begin{bmatrix} p_{0,i,j}^n(x_{i\mp 1/2}, y_j) + p_{1,i,j}^n(x_{i\mp 1/2}, y_j) \\ v_{x,0,i,j}^n(x_{i\mp 1/2}, y_j) + v_{x,1,i,j}^n(x_{i\mp 1/2}, y_j) \\ v_{y,0,i,j}^n(x_{i\mp 1/2}, y_j) + v_{y,1,i,j}^n(x_{i\mp 1/2}, y_j) \\ T_{0,i,j}^n(x_{i\mp 1/2}, y_j) + T_{1,i,j}^n(x_{i\mp 1/2}, y_j) \end{bmatrix} \quad \text{and} \\
\mathbf{w}_{i,j\mp 1/2\pm}^n &= \begin{bmatrix} p_{0,i,j}^n(x_i, y_{j\mp 1/2}) + p_{1,i,j}^n(x_i, y_{j\mp 1/2}) \\ v_{x,0,i,j}^n(x_i, y_{j\mp 1/2}) + v_{x,1,i,j}^n(x_i, y_{j\mp 1/2}) \\ v_{y,0,,ji}^n(x_i, y_{j\mp 1/2}) + v_{y,1,,ji}^n(x_i, y_{j\mp 1/2}) \\ T_{0,i,j}^n(x_i, y_{j\mp 1/2}) + T_{1,i,j}^n(x_i, y_{j\mp 1/2}) \end{bmatrix}.
\end{aligned} \tag{1.40}$$

Chapter 2

Implementation and Verification

2.1 Programming Environment

Implementation of the well-balanced method was carried out using the foam-extend 4.0 fork of the OpenFOAM (Open-Source Field Operation And Manipulation) software project. OpenFOAM was selected as it is a mature and feature-rich platform for computational fluid dynamics, and thus already provides many utilities and functionality for tasks such as pre- and post-processing data, runtime selection of simulation parameters, and managing very generic meshes. It is coded entirely in object-oriented C++, making it also very flexible for extension.

The foam-extend fork was chosen over the standard OpenFOAM distribution as it includes an additional density-based Navier Stokes (DBNS) solver which implements very closely the basic FVM which was to be modified. As well, this DBNS library contains several already programmed numerical fluxes and gradient limiters, such that the focus could remain on developing the well-balanced reconstruction without having to code all of the supporting pieces from scratch.

For all of the simulations, the Rusanov flux [11] was chosen for the numeric flux function (i.e. the approximate Riemann Solver) and the Venkatakrishnan limiter [6, 7] was used for the gradient limiting in the second order schemes. Both of these were used as already implemented in the DBNS library, with modifications only being made in the higher-level classes which called these modules, such that other limiter and flux function implementations could easily be swapped in if desired, using the runtime selectability provided by OpenFOAM.

The Rusanov flux was chosen as it inherently provided sufficient numerical dissipation to keep the simulations stable for all of the cases tested, while the HLLC and Roe flux functions, which are also implemented in the

Table 2.1: Computational times for sample problems in various dimensions comparing the second-order unbalanced and well-balanced schemes.

	CPU time [s]		
Dimension	unbalanced	well-balanced	Ratio
1D	313	1715	5.48
2D	466	1999	4.29
3D	17268	40386	2.34

DBNS package, became unstable for the perturbed standing shock problem described in Section 3.1.2.

The Venkatakrishnan limiter was chosen for its applicability to steady state flows, where the differentiability of its limiter function has been shown to speed convergence to stationary flow solutions. It is noted that some testing with the Barth-Jespersen limiter also produced satisfactory results for the convergence studies, and in general the choice of gradient limiter should not impact on the well-balanced nature of the scheme.

2.1.1 Computational Time

As iterative Newton-Raphson solutions are required by the balanced scheme, this is expected to make it more computationally expensive than the standard methods for a given grid resolution. While the exact difference in compuational cost will depend on the memory requirements and set-up of the problem being simulated, a couple of CPU times are presented in Table 2.1 for representative simulations in 1D, 2D, and 3D, to give an idea of the observed computational cost. These timings include initialization time and writing of final result files so they are only intended as a rough initial comparison between the unbalanced and well-balanced schemes.

It is noted that this work was primarily focused on the development, implementation, and testing of the new well-balanced method, not optimization thereof, so some level of improvement could almost certainly still be achieved over these results.

2.2 Order Verification Study

An order verification study (OVS) was carried out to verify that the implementation matched the theoretically expected convergence rates. For the tests, a piecewise continuous potential function was defined on the 1D domain $x \in [-2, 2]$, composed of two small constant regions at the boundaries

connected by a fifth-order polynomial

$$\phi(x) = \begin{cases} 0, & x \leq -1.5 \\ \dfrac{2}{81}x^5 + \dfrac{5}{27}x^3 + \dfrac{5}{8}x + \dfrac{1}{2}, & -1.5 < x < 1.5 \\ 1, & x \geq 1.5 \end{cases}$$ (2.1)

The constant regions at the domain edges allowed for simple zero-gradient boundary conditions to be used for all non-fixed primitives, and the quintic coefficients were chosen to match also the first and second derivatives (to zero) at the transition points to the constant regions.

The inlet of the flow was set using Dirichlet boundary conditions on T and v_x at $x = 2$ with the values set to the same as those used for the inlet of sub-problem 1 described in Section 3.1 (see there for a more detailed description of how these values are determined). To briefly summarize here, at the inlet one has $p = 0.75, T = 1.05$, and $v_x = -\sqrt{31/199} \approx -0.39$, with adiabatic constant $\gamma = 4/3$ and units such that $c = \rho = 1$. The inlet condition for the pressure is set to zero-gradient at the inlet, as having both it and the velocity fixed caused spurious error in some test cases and was recommended against in the OpenFOAM documentation. At the outlet, all primitives were given homogenous Neumann boundary conditions.

For the initial conditions in the rest of the domain, the value of the density $\rho(x)$ for an equilibrium flow was calculated, and then superimposed with a Gaussian perturbation centred at $x = 0$, given by

$$\Delta\rho(x) = \frac{A}{2\sigma\sqrt{2\pi}} \exp\left[-\frac{1}{2}\left(\frac{x}{\sigma}\right)^2\right].$$ (2.2)

The width of the Gaussian was determined with $\sigma = 0.2$ and the amplitude A was varied to control the maximal magnitude of the perturbation over several series of tests. Once the full $\rho(x)$ function was known, it was used to compute the other initial primitive values throughout the domain. In Fig. 2.1 can be seen an example of these initial conditions as computed for the unperturbed equilibrium flow test.

Results of the simulations were characterized using the average absolute error magnitude, which is calculated as the normalized L1 norm of the error

$$Err_1 = \frac{1}{N}\sum_{i=1}^{N}|\rho_i - \rho_{i,\text{ref}}|,$$ (2.3)

where ρ_{ref} is a reference solution that is obtained either from exact calculation of the unperturbed equilibrium flow values, or from an overkill high-resolution simulation computed using $N = 21870$ cells and the second-order well-balanced scheme for the test cases with the Gaussian perturbation. For the OVS, the number of cells is progressively tripled from $N = 10$
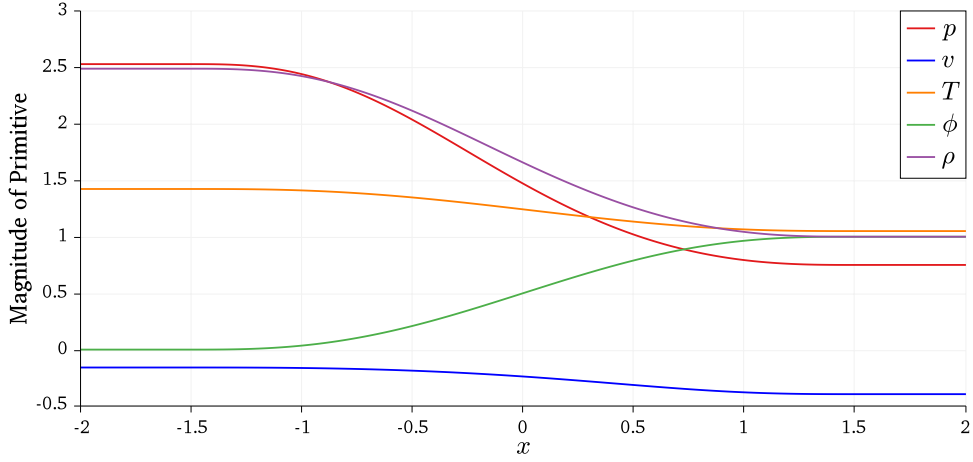
Figure 2.1: Magnitude profiles of the primitive values, density, and potential field at the initial time for the unperturbed equilibrium convergence test.

to $N = 7290$ and the intra-step order of accuracy is computed by determining the slope of the line connecting the error values of each adjacent pair of simulations using successively refined grids on a log-log plot of Err_1 vs. Δx.

Tripling was used such that when refining the grid, each cell would be perfectly split in three, and thus the position of the cell centre for the newly created middle cell would align exactly with the cell centre for the original coarse cell. Therefore, no interpolation is required to compare the cell centre values with the solutions obtained at any of the finer resolutions, and in particular the reference solution contains a value precisely at the location of each cell centre of every other grid resolution tested.

All convergence simulations were run to a final time of $t = 1$, which was sufficient for the perturbations to have travelled significantly through the domain but still be mostly entirely contained within it.

2.2.1 Equilibrium Flow

The results of the first series of simulations at equilibrium, i.e. with $A = 0$, are tabulated in Table 2.2 and demonstrate very close agreement to the expected first- and second-order accuracy for the unbalanced schemes. For the well-balanced schemes, the average error is at the level of the machine precision for all grid resolutions, demonstrating the precise maintenence of the equilibrium flow irrespective of the number and size of the grid cells. This serves as a strong empirical verification of the precise matching between the source and flux term discretizations in the (1.4) balance law for steady states, i.e. it truly is "well-balanced".

In Fig. 2.2 can be seen a visual representation of the same data from Table 2.2,

Table 2.2: L1 error of the density and intra-step order of accuracy for the first- and second-order unbalanced/well-balanced schemes with no perturbation, i.e. $A = 0$.

| N | First | | Second | |
	Err_1	Order	Err_1	Order
10	8.54e-02/4.04e-15		2.59e-02/4.04e-15	
30	2.89e-02/5.20e-15	0.99/-	3.16e-03/5.20e-15	1.91/-
90	9.77e-03/4.08e-15	0.99/-	3.44e-04/4.09e-15	2.02/-
270	3.27e-03/3.63e-15	1.00/-	3.77e-05/3.66e-15	2.01/-
810	1.09e-03/2.96e-15	1.00/-	4.17e-06/5.05e-15	2.00/-
2430	3.64e-04/3.78e-14	1.00/-	4.63e-07/5.20e-14	2.00/-
7290	1.21e-04/1.04e-14	1.00/-	5.14e-08/1.37e-14	2.00/-
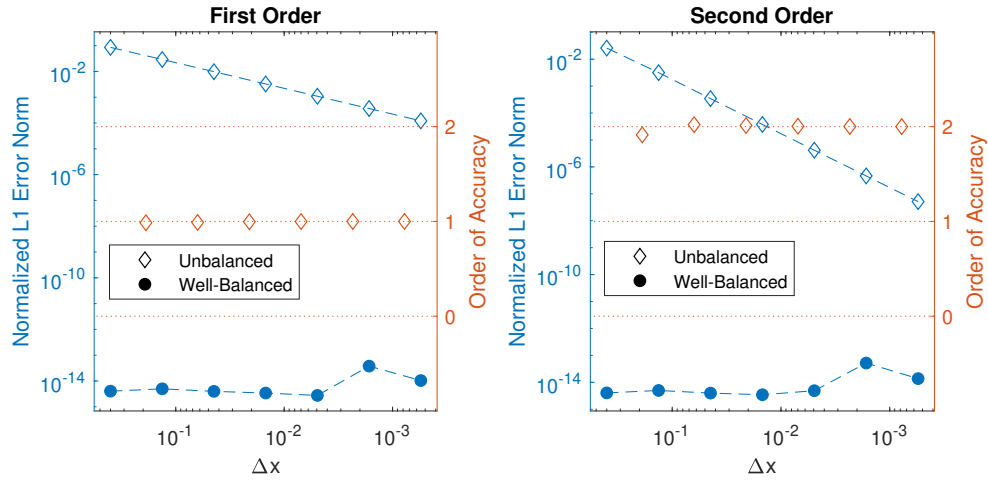
Figure 2.2: L1 error of the density (in blue with dashed line) and intra-step order of accuracy (in red with no line) for the first- and second-order unbalanced and well-balanced schemes with no perturbation, i.e. $A = 0$.

making clear both the clean asymptotic convergence of the standard schemes as well as the many orders of magnitude greater accuracy achieved by the well-balanced method in simulating the stationary flow.

2.2.2 Gaussian Perturbation

Next is a series of tests using a 'medium' amplitude Gaussian perturbation with $A = 0.1$, with the initial and final density profiles of the reference solution shown in Fig. 2.3. This amplitude was chosen as it is large enough to be clearly resolved by all four combinations of first/second-order and
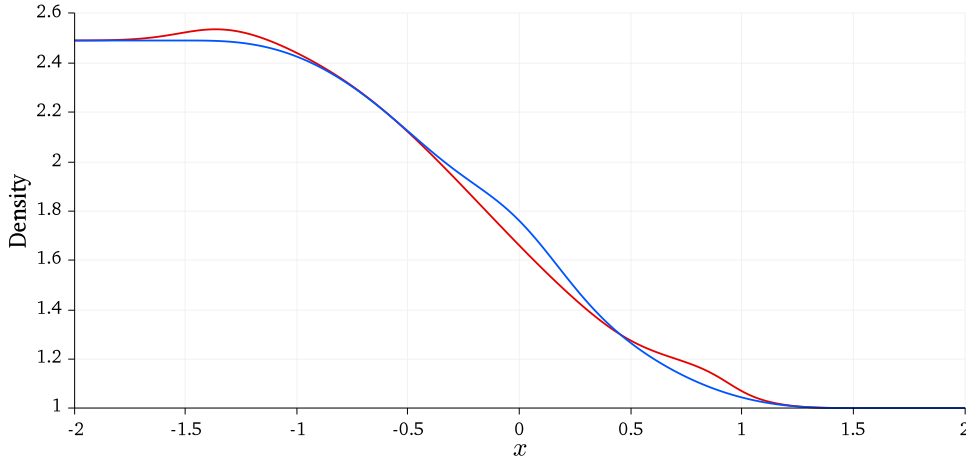
Figure 2.3: Density profiles at the initial time (blue line) and final time (red line) of the reference simulation for the medium amplitude $(A = 0.1)$ convergence test, showing no discontinuities.

un/well-balanced schemes, as seen in the table where all average errors are smaller than A. However, the amplitude was still small enough to ensure that the final solution remained smooth and does not yet present any steepening of flow features into discontinuities. Data from the convergence tests are presented in Table 2.3 and visualized in Fig. 2.4.

It can be seen that the expected orders of accuracy are observed for the respective first- and second-order schemes where the graphs are in the asymptotic regime. In the second-order case it is noted that the results become abruptly non-linear for the smallest 1-2 grid spacings, due to the use of a reference solution which is itself only computed with the second-order well-balanced scheme using thrice as many cells as the final resolution presented on the plots. Thus the magnitude of errors still present in this reference becomes comparable to the errors in the final steps of the grid refinement, and so the linear convergence breaks down.

2.2.3 Small Amplitude Perturbation

In all cases for the medium amplitude, the well-balanced scheme is observed to have slightly lower errors than the unbalanced scheme, although the difference is relatively minor in this instance where the perturbation is much larger than the errors in the underlying equilibrium observed in the first convergence series with no perturbation. As such, we are interested in observing what happens for a perturbation amplitude that is quite small, comparable to or less than the average errors observed for the unbalanced scheme on the equilibrium flow. Therefore a third convergence series was carried out using a very small amplitude perturbation with $A = 10^{-4}$, the results of which can be found in Table 2.4 and Fig. 2.5.

Table 2.3: L1 error of the density and intra-step order of accuracy for the first- and second-order unbalanced/well-balanced schemes with medium perturbation amplitude $A = 0.1$.

| N	First		Second	
	Err_1	Order	Err_1	Order
10	8.63e-02/1.23e-02		2.72e-02/7.51e-03	
30	2.90e-02/9.68e-03	0.99/0.21	5.76e-03/3.78e-03	1.41/0.62
90	1.05e-02/5.63e-03	0.93/0.49	7.30e-04/5.29e-04	1.88/1.79
270	4.01e-03/2.61e-03	0.87/0.70	7.37e-05/5.34e-05	2.09/2.09
810	1.48e-03/1.01e-03	0.91/0.86	8.68e-06/5.89e-06	1.95/2.01
2430	5.14e-04/3.58e-04	0.96/0.95	2.97e-06/8.48e-07	0.98/1.76
7290	1.74e-04/1.22e-04	0.98/0.98	2.62e-06/5.80e-07	0.11/0.35
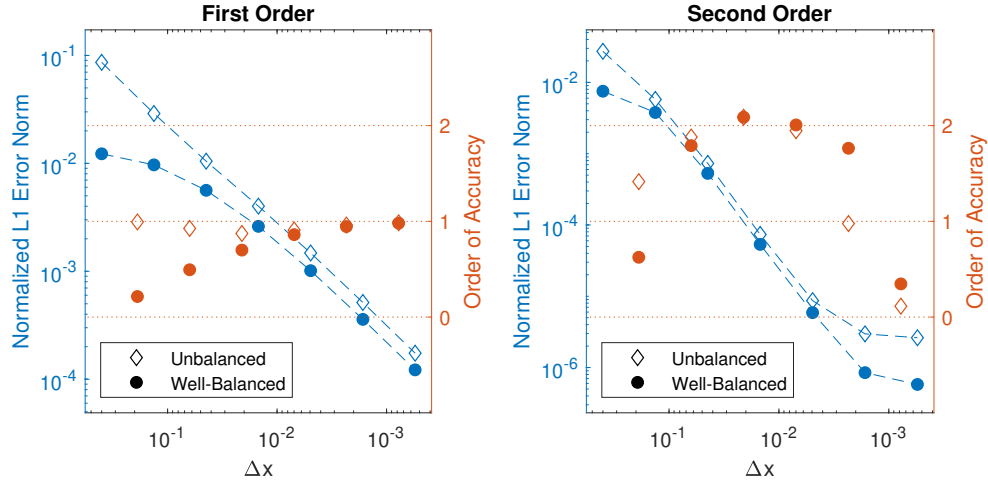
Figure 2.4: L1 error of the density (in blue with dashed line) and intra-step order of accuracy (in red with no line) for the first- and second-order unbalanced and well-balanced schemes with medium perturbation amplitude $A = 0.1$.

Table 2.4: L1 error of the density and intra-step order of accuracy for the first- and second-order unbalanced/well-balanced schemes with very small perturbation amplitude $A = 10^{-4}$.

N	First		Second	
	Err_1	Order	Err_1	Order
10	8.54e-02/1.22e-05		2.59e-02/7.71e-06	
30	2.89e-02/9.73e-06	0.99/0.21	3.17e-03/3.93e-06	1.91/0.61
90	9.77e-03/5.71e-06	0.99/0.49	3.44e-04/5.42e-07	2.02/1.80
270	3.27e-03/2.67e-06	1.00/0.69	3.77e-05/5.36e-08	2.01/2.11
810	1.09e-03/1.04e-06	1.00/0.86	4.17e-06/5.91e-09	2.00/2.01
2430	3.64e-04/3.67e-07	1.00/0.95	4.64e-07/8.39e-10	2.00/1.78
7290	1.21e-04/1.25e-07	1.00/0.98	5.28e-08/5.69e-10	1.98/0.35
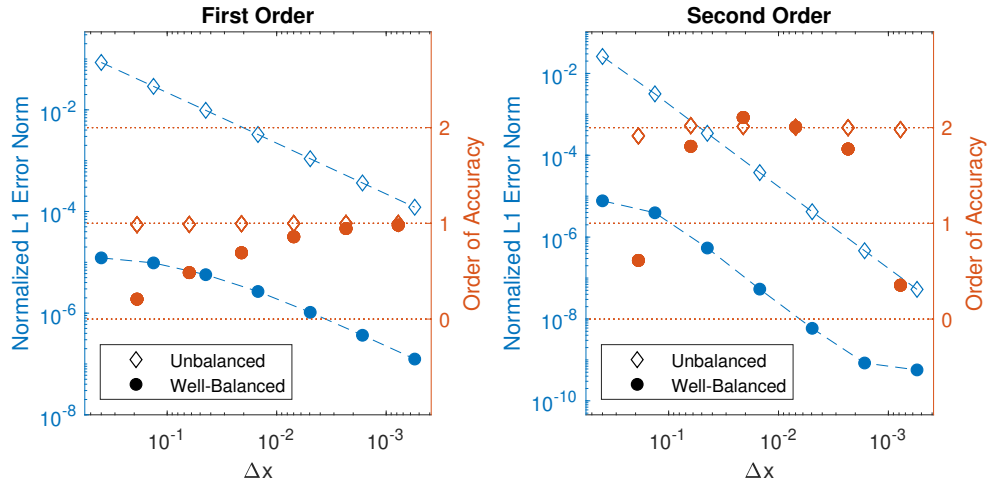
Figure 2.5: L1 error of the density (in blue with dashed line) and intra-step order of accuracy (in red with no line) for the first- and second-order unbalanced and well-balanced schemes with very small perturbation amplitude $A = 10^{-4}$.

From the results, it is clear that the average error of the unbalanced scheme is much larger than the perturbation amplitude for all studied grid resolutions in the first-order case, and and even for the second-order scheme requires a fairly significant level of refinement before the error drops low enough for the perturbation to possibly be well resolved. The order of the convergence is of course still correct in both instances, but this is essentially just the same convergence towards the equilibrium as in the $A = 0$ case, since the large magnitude of the errors compared to the perturbation amplitude mean that the deviation is not meaningfully perceived or simulated by the scheme over much of the parameter space.

By contrast, the well-balanced scheme exhibits average errors much smaller than the perturbation amplitude, with even the least resolved first-order simulation already having almost a full order of magnitude smaller error. Observed orders of convergence are the same as for the unbalanced scheme, but as exemplified visually in Fig. 2.5, the absolute size of the errors is many orders of magnitude less for the well-balanced scheme. No level of grid refinement studied was able to get the first-order unbalanced scheme to the accuracy of its well-balanced counterpart, and it required approximately 3^3 times more grid cells in the second-order tests to match the observed accuracy there. This demonstrates the potentially massive savings in computational cost provided by the well-balanced method for simulating small perturbations, especially in 2D or 3D simulations where the benefits would be compounded along each additional dimension.

2.2.4 Discontinuous Flow

Lastly, a large $A = 2$ amplitude perturbation was used to investigate the performance of the schemes when steepened discontinuities become present in the solution. As seen in Fig. 2.6, the density profiles at the final time have developed clear discontinuities from the initially smooth profile. The results of the convergence tests for this amplitude are given in Table 2.5 and reveal that the order of accuracy has now dropped to first-order for all schemes, because the gradient limiting means that the normally second-order schemes are reduced to first-order accuracy at the sharp transition points, and so this observed reduction in the convergence order agrees with the expected behaviour of such TVD limited reconstruction methods.

Fig. 2.7 shows almost perfect overlap of the errors of the un/well-balanced schemes. As mentioned in Section 2.1.1 the well-balanced scheme is more computationally expensive than the standard method for a given grid resolution, and combined with the earlier medium and small amplitude results, this implies that the use of the well-balanced scheme is only justified for simulations involving deviations from the equilibrium flow that are smaller than or comparable to the error in the equilibrium state for the standard
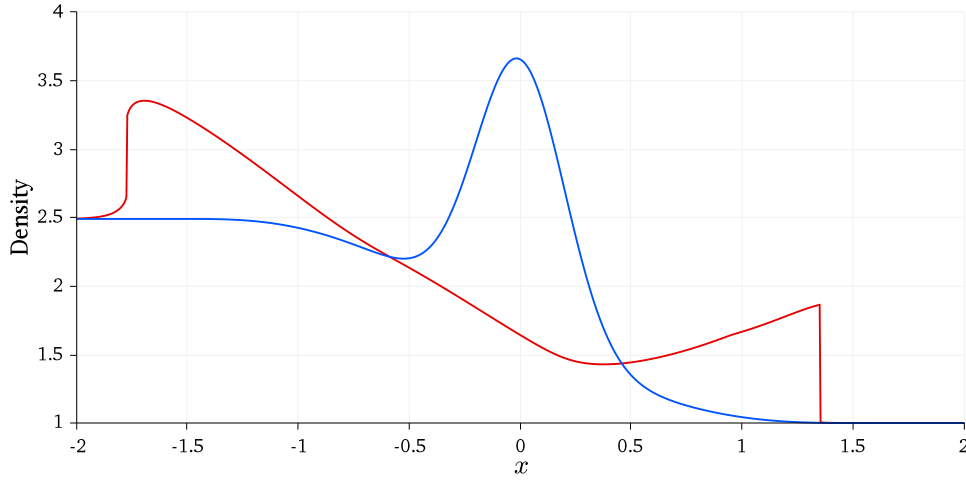
Figure 2.6: Density profiles at the initial time (blue line) and final time (red line) of the reference simulation for the large amplitude $(A = 2)$ convergence test, showing clear discontinuities.

Table 2.5: L1 error of the density and intra-step order of accuracy for the first- and second-order unbalanced/well-balanced schemes with very large perturbation amplitude $A = 2$.

N	First Err_1	Order	Second Err_1	Order
10	2.12e-01/1.96e-01		1.13e-01/1.13e-01	
30	1.43e-01/1.44e-01	0.36/0.28	5.06e-02/5.10e-02	0.74/0.73
90	8.04e-02/7.93e-02	0.52/0.54	1.75e-02/1.75e-02	0.97/0.97
270	3.69e-02/3.66e-02	0.71/0.70	5.26e-03/5.26e-03	1.09/1.10
810	1.50e-02/1.48e-02	0.82/0.83	1.88e-03/1.88e-03	0.94/0.93
2430	5.88e-03/5.80e-03	0.85/0.85	5.86e-04/5.82e-04	1.06/1.07
7290	2.18e-03/2.15e-03	0.90/0.90	2.00e-04/1.83e-04	0.98/1.05

scheme. For such cases, the machine precision accuracy of the equilibrium for the balanced scheme means the perturbation can be simulated with a (potentially much) coarser grid, thus countering the higher computational cost per cell to result in overall savings of required effort for a given level of accuracy.

For all amplitudes, a good agreement is seen between the experimental results and the theoretically expected orders of accuracy, providing a solid verification of the correct implementation of the new well-balanced scheme.
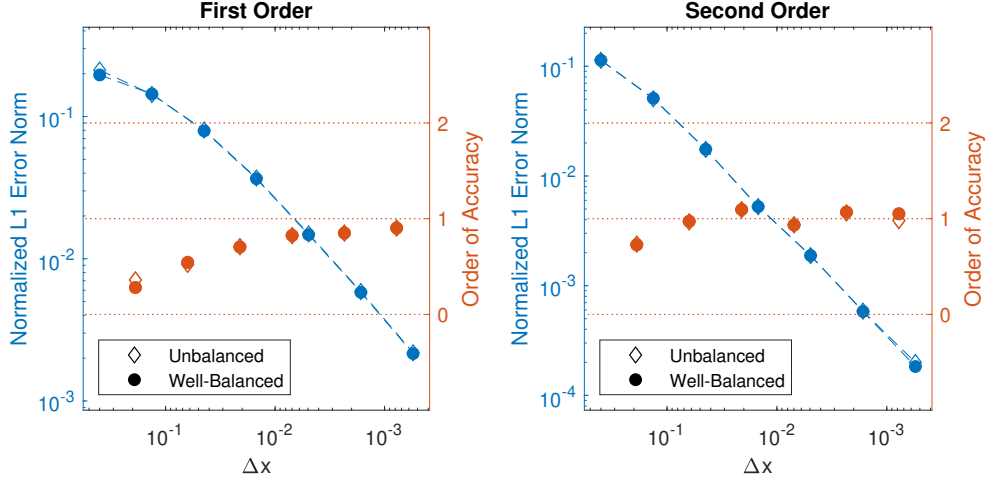
Figure 2.7: L1 error of the density (in blue with dashed line) and intra-step order of accuracy (in red with no line) for the first- and second-order unbalanced and well-balanced schemes with large perturbation amplitude $A = 2$.

2.3   3D Polytrope

With the formal accuracy now demonstrated for regular 1D geometries, a higher dimensional test was carried out using a simple astrophysical problem. The 3D polytrope example from KM14 was chosen, to also illustrate the recovery of the hydrostatic case by the newly extended scheme. This problem simulates a hydrostatic configuration of adiabatic gases held together in a sphere by self-gravitation, according to the spherical equilibrium

$$\frac{\mathrm{d}p}{\mathrm{d}r} = -\rho \frac{\mathrm{d}\phi}{\mathrm{d}r}, \tag{2.4}$$

and Poisson's equation in spherical symmetry

$$\frac{1}{r^2} \frac{\mathrm{d}}{\mathrm{d}r} \left(r^2 \frac{\mathrm{d}\phi}{\mathrm{d}r} \right) = 4\pi G \rho, \tag{2.5}$$

with the radial variable and gravitational constant as r and G, respectively.

Using the polytropic equation of state (1.14), one can combine Eqs. (2.4) and (2.5) into the single Lane-Emden equation

$$\frac{1}{r^2} \frac{\mathrm{d}}{\mathrm{d}r} \left(r^2 \gamma K \frac{\mathrm{d}\phi}{\mathrm{d}r} \right) = -4\pi G \rho, \tag{2.6}$$

which has analytic solutions for three adiabatic constants ($\gamma = 6/5, 2, \infty$). For the following tests $\gamma = 2$ will therefore be used, as neutron stars can be modelled by $\gamma \in [2, 3]$ and an analytic solution exists.

This then gives the following analytic gravitational potential and primitive variable profiles

$$\phi(r) = -2K\rho_c \frac{\sin(\alpha r)}{\alpha r}, \tag{2.7}$$

$$\rho(r) = \rho_c \frac{\sin(\alpha r)}{\alpha r}, \tag{2.8}$$

$$p(r) = K\left(\rho_c \frac{\sin(\alpha r)}{\alpha r}\right)^2, \tag{2.9}$$

$$T(r) = \frac{K\rho_c}{R} \frac{\sin(\alpha r)}{\alpha r}, \tag{2.10}$$

where ρ_c is the density at the centre of the polytrope, R is the specific gas constant, and

$$\alpha = \sqrt{\frac{4\pi G}{2K}}. \tag{2.11}$$

Note that the configuration is hydrostatic, so the velocity profile is simply $v(r) = 0$ everywhere. The model constants are set as $K = G = \rho_c = 1$ and $R = 5/7$.

The polytrope was simulated over a spherical domain of radius $r = 0.5$ centred at the origin. Unstructured tetrahedral meshes with varying numbers of cells N were generated using the Delauney algorithm of Gmsh, followed by mesh optimization with both the standard Gmsh and Netgen optimizers in the Gmsh package. Illustrations of the two coarsest of these meshes are shown in Fig. 2.8. Initial field profiles were simply set using the analytic solutions. Dirichlet boundary conditions were used for all fields except the velocity, and were fixed to the analytic values, with the velocity then given a homogenous Neumann boundary condition.

Results of the simulations are given in Table 2.6, again using the L1 error norm (2.3) of the density to characterize the deviation from the analytic equilibrium. All simulations were run to a final time $t = 1$ with a timestep $\Delta t = 0.001$ for a total of 1000 timesteps.

Measuring the spatial order of accuracy for an unstructured mesh is a much more complicated problem than for a regular cartesian grid, as each cell can have its own size and shape. Therefore a characteristic length scale must be specified for each tested mesh, in order to approximate the order of accuracy for the convergence of the solutions.

In this study, such a characteristic length, denoted h, was computed by using the volume of the largest mesh cell to determine the side length of a regular tetrahedron of that volume, with that side length then multiplied by the largest aspect ratio of the cells in the mesh. It is noted that this h is not intended to represent an actual physical length in the mesh, but to provide

$N\!=\!4144$ $N\!=\!28036$
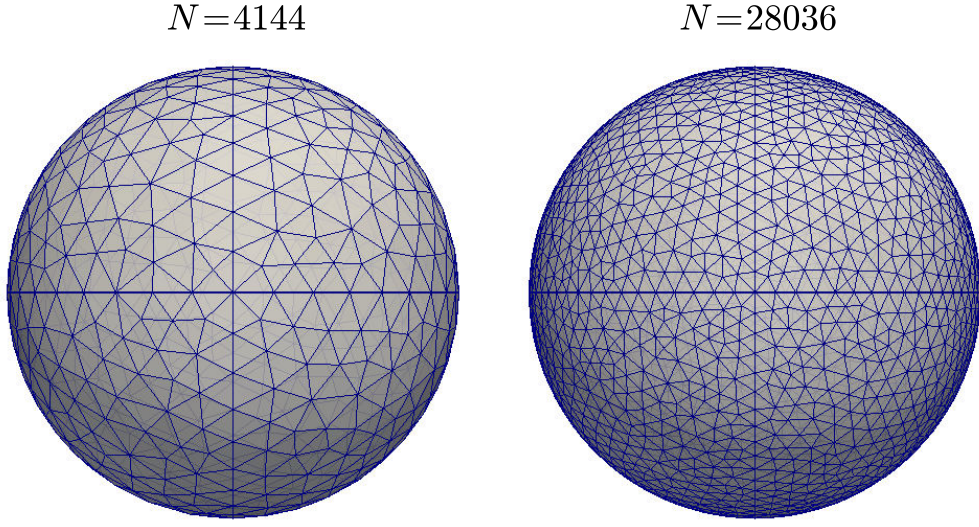
Figure 2.8: Illustrations of the two coarsest meshes generated on a 3D sphere of radius $r = 0.5$ centred at the origin, showing the unstructured tetrahedal mesh and its refinement.

Table 2.6: L1 error of the density and approximate intra-step order of accuracy for the first- and second-order unbalanced/well-balanced schemes for the 3D polytrope on tetrahedral meshes with N cells and characteristic length h.

N	h	First		Second	
		Err_1	Order	Err_1	Order
4144	0.585	8.17e-03/1.23e-15		4.22e-04/1.31e-15	
28036	0.327	6.02e-03/1.22e-15	0.54/-	2.06e-04/1.29e-15	1.24/-
233064	0.177	3.54e-03/1.23e-15	0.87/-	1.07e-04/1.37e-15	1.07/-
1857454	0.097	1.94e-03/1.24e-15	1.01/-	6.04e-05/1.99e-15	0.96/-

a single metric which takes into account both the size and quality of the cells present in the mesh, and which should scale comparably between meshes generated using the same algorithm.

Analyzing the results revealed machine precision deviation from the analytic equilibrium for the new first- and second-order well-balanced schemes on all mesh sizes, confirming the well-balanced properties even on an unstructured tetrahedral mesh. The standard scheme, by contrast, produces spurious perturbations, which do converge to the analytic solution with increasing mesh resolution. For the first-order scheme, the approximate order of accuracy approaches the expected value of unity as the mesh is refined, while for the second-order scheme the order actually decreases towards unity as well for higher N, although the magnitude of the error is

lower than for the first-order scheme.

Some of this deviation from the expected order may be due to the approximate nature of the characteristic length used for the analysis, but it has also been shown by Roe [16] that local truncation error for some FVMs is only first-order accurate for very irregular triangular meshes. Therefore this first-order accuracy on tetrahedral meshes may not be entirely surprising, although Lindquist and Giles [17] and Giles [18] have shown that for some triangular meshes global second-order accuracy is possible, so perhaps for a higher-quality mesh and more precise characteristic length a better convergence order could be demonstrated. However, as the well-balanced schemes, not the standard schemes, are the focus of this thesis, such further studies are not undertaken here.

Chapter 3

Application: SASI Toy Problem

As mentioned at the beginning of Chapter 1, the simple toy model of F09 [2] and SFF09 [3] was chosen as a useful initial application of our well-balanced method to the SASI. The salient details from those papers are reproduced here.

The basic set-up of the problem consists of a 2D domain with periodic boundary conditions on both edges in the x-direction and three distinct flow regions in the y-direction. First is a supersonic inflow, which is transitioned by a shock front at $y = y_{\mathrm{sh}}$ to subsonic speeds in the second region. This is then separated from a third region (also subsonic) by a potential step at $y = y_\nabla$ which further decelerates the flow and provides a simple model of matter slowing as it nears the surface of the accreting object. Following the notation of SFF09, we will denote quantities in the supersonic region before the shock with a subscript '1', in the interior region between the shock and potential step with 'in', and in the outflow region past the step with 'out'.

A schematic view of the problem domain with all three regions can be seen on the left side of Fig. 3.1, with the right side showing how the overall scenario is then split into two sub-problems for initial simulation. This separation greatly simplifies the introduction of specific advective and acoustic perturbations to appropriate locations in the interior of the domain, making it much easier to see the interactions of these disturbances at the boundaries (the shock and potential step) between the various flow regions. Overall, this provides a much simplified analogue for simulations to study the mechanisms at play during the inflow, decceleration, and accretion of matter in a collapsing star before supernova.

General parameters of the model problem will be presented next, followed by specific information for the potential step and stationary shock, computed separately as sub-problems 1 and 2, respectively.
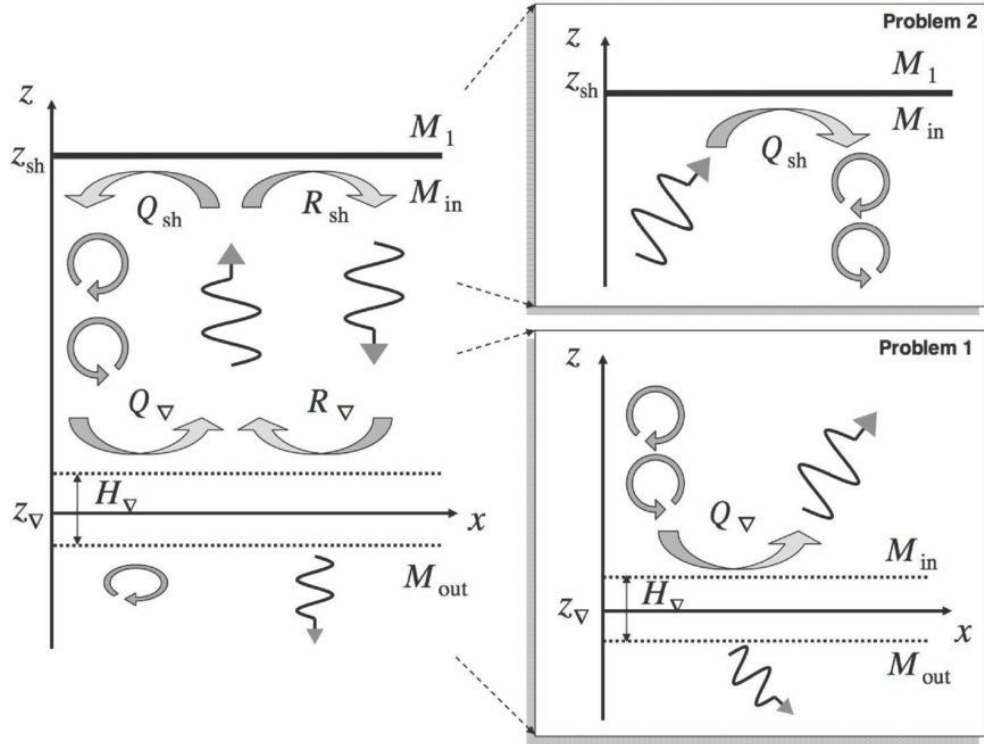
Figure 3.1: This image is taken directly from SFF09 [3]. On the left is a schematic diagram of the full toy problem for the SASI, which is then broken into two sub-problems on the right. Circular arrows represent advective vorticity waves while wavy arrows denote acoustic pressure waves. The coupling efficiencies denote the strength of coupling between acoustic and advective waves (Q_{sh}, Q_{∇}) and the reflection of purely acoustic waves (R_{sh}, R_{∇}).

3.1 Problem Set-up

The general flow problem to be studied is essentially a 1D flow when at equilibrium, with the periodicity in the x-direction mimicking an infinitely wide flow and all variation occuring in the y-direction. Simulating this problem in 2D then, is done purely for studying the perturbations to this equilibrium flow, thus allowing more interesting perturbations and potential higher-dimenensional features to also be realized.

An ideal gas with an adiabatic constant $\gamma = 4/3$ was simulated, the extent of the domain in the x-direction is denoted as L_x, and the entropy of the fluid is defined as

$$S \equiv \frac{\log\left(p/\rho^{\gamma}\right)}{\gamma - 1}. \tag{3.1}$$

Beginning with a Mach number of $\mathcal{M}_1 = 5$ at the inflow, one can then compute the relations of flow values across the shock as defined by the

Rankine-Hugoniot conditions

$$\mathcal{M}_{\text{in}} = \sqrt{\frac{2 + (\gamma - 1)\mathcal{M}_1^2}{2\gamma\mathcal{M}_1^2 - \gamma + 1}}, \tag{3.2}$$

$$\frac{v_1}{v_{\text{in}}} = \frac{(\gamma + 1)\mathcal{M}_1^2}{2 + (\gamma - 1)\mathcal{M}_1^2}, \tag{3.3}$$

$$\frac{\rho_1}{\rho_{\text{in}}} = \frac{v_{\text{in}}}{v_1}, \tag{3.4}$$

where $v_{\text{in}} = -\mathcal{M}_{\text{in}} c_{\text{in}}$ and the interior Mach number is found to be $\mathcal{M}_{\text{in}} = \sqrt{31/199} \approx 0.39$.

A hyperbolic tangent function is used to provide a smooth step-like external potential field centred at $y_\nabla = 0$ extant over an approximate width H_∇, with the exact function given by

$$\phi(y) = \frac{\Delta\phi}{2}\left[\tanh\left(\frac{y - y_\nabla}{H_\nabla/2}\right) + 1\right], \tag{3.5}$$

where the step size $\Delta\phi$ is set based on the ratio of the sound speeds $c_{\text{in}}/c_{\text{out}}$ in the constant regions surrounding the step, and can be computed as

$$\Delta\Phi = \left(\frac{\mathcal{M}_{\text{out}}^2}{2} + \frac{1}{\gamma - 1}\right)c_{\text{out}}^2 - \left(\frac{\mathcal{M}_{\text{in}}^2}{2} + \frac{1}{\gamma - 1}\right)c_{\text{in}}^2. \tag{3.6}$$

For all simulations, the ratio $c_{\text{in}}^2/c_{\text{out}}^2 = 0.75$ was used, and the step width was chosen such that $H_\nabla/H = 0.1$ where $H \equiv y_{\text{sh}} - y_\nabla$ is defined to be the distance between the shock and the middle of the potential step.

A reference timescale for the advective-acoustic cycle is used to normalize the simulation times, and is calculated as

$$\tau_{\text{aac}} \equiv \frac{1}{1 - \mathcal{M}_{\text{in}}}\frac{H}{|v_{\text{in}}|}. \tag{3.7}$$

Units for all quantities are chosen to ensure that $c_{\text{in}} = \rho_{\text{in}} = H = 1$. Using the relation $p = \rho c^2/\gamma$ we can compute the other primitive values in the interior region as $p_{\text{in}} = 0.75$ and $T_{\text{in}} = 1.05$ and the reference timescale as $\tau_{\text{aac}} \approx 4.2$. A wavenumber $k_x = 2\pi/L_x$ is used to define linear perturbations of the flow, where $L_x = 4$, along with a temporal frequency defined as $\omega_0 = 4\pi/\tau_{\text{aac}}$.

For both sub-problems a 4×4 square domain is used, divided into a uniform number $N_x = N_y = 400$ of square grid cells in both dimensions. This gives a uniform grid spacing of $\Delta x = \Delta y = 10^{-2}$.

3.1.1 Sub-Problem 1: Potential Step

For the first sub-problem, the potential step positioned at $y_\nabla = 0$ is the only flow feature simulated on a square domain defined on $y \in [-1,3]$, $x \in [0,4]$. Inflow occurs at the upper $y = 3$ boundary, defined using Dirichlet conditions, and zero-gradient conditions are imposed at the $y = -1$ outflow boundary. Initial conditions are determined by computing the equilibrium flow for the given inlet primitive values over the potential field. By defining also a vertical wavenumber $k_y = \omega_0 / v_{\text{in}}$ the perturbations injected at the inlet are given by the equations

$$\delta S \equiv \epsilon_S \cos\left(-\omega_0 t + k_x x + k_y y\right), \tag{3.8}$$

$$\frac{\delta \rho}{\rho_{\text{in}}} \equiv \exp\left(-\frac{\gamma - 1}{\gamma} \delta S\right) - 1, \tag{3.9}$$

where $\epsilon_S = 10^{-3}$ is the amplitude of the generated entropy waves.

These incoming waves are desired to be at pressure equilibrium ($\delta p = 0$), and so from the equation of state one can then determine the consistent temperature perturbation

$$\frac{\delta T}{T_{\text{in}}} = \left(1 + \frac{\delta \rho}{\rho_{\text{in}}}\right)^{-1} - 1 = \exp\left(\frac{\gamma - 1}{\gamma} \delta S\right) - 1. \tag{3.10}$$

Deviations to the 2D velocity components are given as

$$\delta v_x \equiv \frac{k_x \omega_0 c_{\text{in}}^2}{\omega_0^2 + k_x^2 v_{\text{in}}^2} \frac{\delta S}{\gamma} \quad \text{and} \quad \delta v_y \equiv -\frac{k_x^2 v_{\text{in}} c_{\text{in}}^2}{\omega_0^2 + k_x^2 v_{\text{in}}^2} \frac{\delta S}{\gamma}, \tag{3.11}$$

which result in the generation of the following vorticity waves

$$\delta w_y = -\frac{k_x c_{\text{in}}^2}{v_{\text{in}}} \frac{\epsilon_S}{\gamma} \sin\left(-\omega_0 t + k_x x + k_y y\right). \tag{3.12}$$

These waves, which are injected only at the inlet, are allowed to travel through the interior region towards the potential step, and then any resultant coupling of the vorticity waves into reflected pressure waves is observed.

3.1.2 Sub-Problem 2: Standing Shock

For the second sub-problem, only the shock front positioned at $y_{\text{sh}} = 1$ is simulated, with the square domain now defined on $y \in [-2,2]$, $x \in [0,4]$. Inflow is now supersonic and again set with Dirichlet boundaries at $y = 2$, although the outflow conditions at $y = -2$ are different from sub-problem 1. Homogoneous Neumann conditions are still used initially while no perturbations are present in the system, to allow the shock to "settle in" and

any waves generated by this settling process to propagate cleanly out of the system. Once a steady state is reached, however, the outflow conditions are changed to be also Dirichlet in order to inject the desired perturbations into the domain from the outflow boundary. The time at which this "switching on" of the injected perturbations occurs is labeled as the starting time $\tau = 0$ for the simulations. Initial conditions are in this case determined purely by the Rankine-Hugoniot conditions given earlier to define the shock, since the potential field is now constant throughout the entire domain.

Vorticity-free pressure perturbations are generated for this sub-problem, and by defining a new vertical wavenumber

$$k_y^{\pm} = \frac{\omega_0}{c_{\text{in}}} \frac{\mathcal{M}_{\text{in}} \mp \mu}{1 - \mathcal{M}_{\text{in}}^2}, \tag{3.13}$$

and density perturbation amplitude $\epsilon_\rho = 10^{-3}$, one has the equations for the perturbations injected at the outlet as

$$\frac{\delta\rho}{\rho_{\text{in}}} \equiv \left(\frac{1 + \mu\mathcal{M}_{\text{in}}}{1 - \mathcal{M}_{\text{in}}^2} \right) \epsilon_\rho \cos\left(-\omega_0 t + k_x x + k_y^- y \right), \tag{3.14}$$

$$\frac{\delta p}{p_{\text{in}}} \equiv \left(1 + \frac{\delta\rho}{\rho_{\text{in}}} \right)^{\gamma} - 1, \tag{3.15}$$

where one can again use the equation of state to determine the consistent temperature deviation

$$\frac{\delta T}{T_{\text{in}}} = \left(1 + \frac{\delta\rho}{\rho_{\text{in}}} \right)^{\gamma-1} - 1. \tag{3.16}$$

Velocity perturbations for these purely acoustic pressure waves are given by

$$\delta v_x \equiv \left(\frac{k_x c_{\text{in}}^2}{\omega_0} \right) \epsilon_\rho \cos\left(-\omega_0 t + k_x x + k_y^- y \right), \tag{3.17}$$

$$\delta v_y \equiv \left(\frac{\mu + \mathcal{M}_{\text{in}}}{1 - \mathcal{M}_{\text{in}}^2} \right) c_{\text{in}} \epsilon_\rho \cos\left(-\omega_0 t + k_x x + k_y^- y \right), \tag{3.18}$$

where the parameter μ is simply used for convenience and expands as

$$\mu \equiv \sqrt{1 - \frac{k_x^2 c_{\text{in}}^2}{\omega_0^2} \left(1 - \mathcal{M}_{\text{in}}^2 \right)}. \tag{3.19}$$

These waves then propagate towards the shock front, and any resultant generation of reflected vorticity waves is measured.

3.2 Numerical Results

Results of simulations for the two sub-problems are presented next, comparing the results to those obtained in F09 and SFF09.

3.2.1 Sub-Problem 1

In Fig. 3.2 can be seen the numerical results obtained for the potential step problem using the well-balanced scheme, with data presented in a manner similar to Fig. 2 in SFF09 to allow easy comparison. At three successive times, the first before and the second and third after the injected entropy-/vorticity waves have reached the potential step, are shown the specific vorticity on the left and the normalized pressure perturbation on the right. Excellent qualitative agreement is seen to the corresponding figure in SFF09. Before the incident wave reaches the step, the right hand column is largely free of any perturbations, with reflected and (less strong) transmitted pressure deviations observed only as the incident wave passes through the deceleration zone centred at $y_\nabla = 0$, illustrating clear generation of acoustic waves as the incoming vorticity wave is decelerated at the potential step. It is also clear to see that in comparison to the figure in SFF09, there is essentially no spurious deviation from the equilibrium flow observed over the potential step itself in our simulation with the new well-balanced scheme, at any of the timepoints.

In order to obtain a more quantitative comparison, the amplitude of the acoustic feedback was measured, using a Fourier transform of the induced pressure perturbation, over one full wave period $T \equiv 2\pi/\omega_0$, with the transform defined by

$$\hat{\delta p}_0 = \frac{2}{T} \int_0^T \delta p e^{i\omega_0 t} \mathrm{d}t. \tag{3.20}$$

By assuming that the generated acoustic wave is advected away from the potential step relatively unchanged, in essence invoking Taylor's frozen turbulence hypothesis, the data for the perturbation was taken from the final timepoint ($\tau = 3.13$) by measuring over a full spatial wavelength. These values are then cast back to the time domain by pairing the datapoints with the correct Fourier frequencies for the integration, as if they had in fact been taken at a single spatial point over the above time interval. With this, the efficiency of the acoustic feedback from the incoming entropy wave is calculated to be

$$\left(\hat{\delta p}_0 / p_{\mathrm{in}} \right) / \delta S = 0.338.$$

In order to have a good value for comparison, the expected value was read off the analytic solution line of Fig. 3 in SFF09 for the simulated frequency of $\omega_0 \tau_{\mathrm{aac}} / 2\pi = 2$ and determined to be approximately $\left(\hat{\delta p}_0 / p_{\mathrm{in}} \right) / \delta S = 0.32$. This therefore shows excellent agreement between our simulated results and the expected value from the linear analysis undertaken in F09.
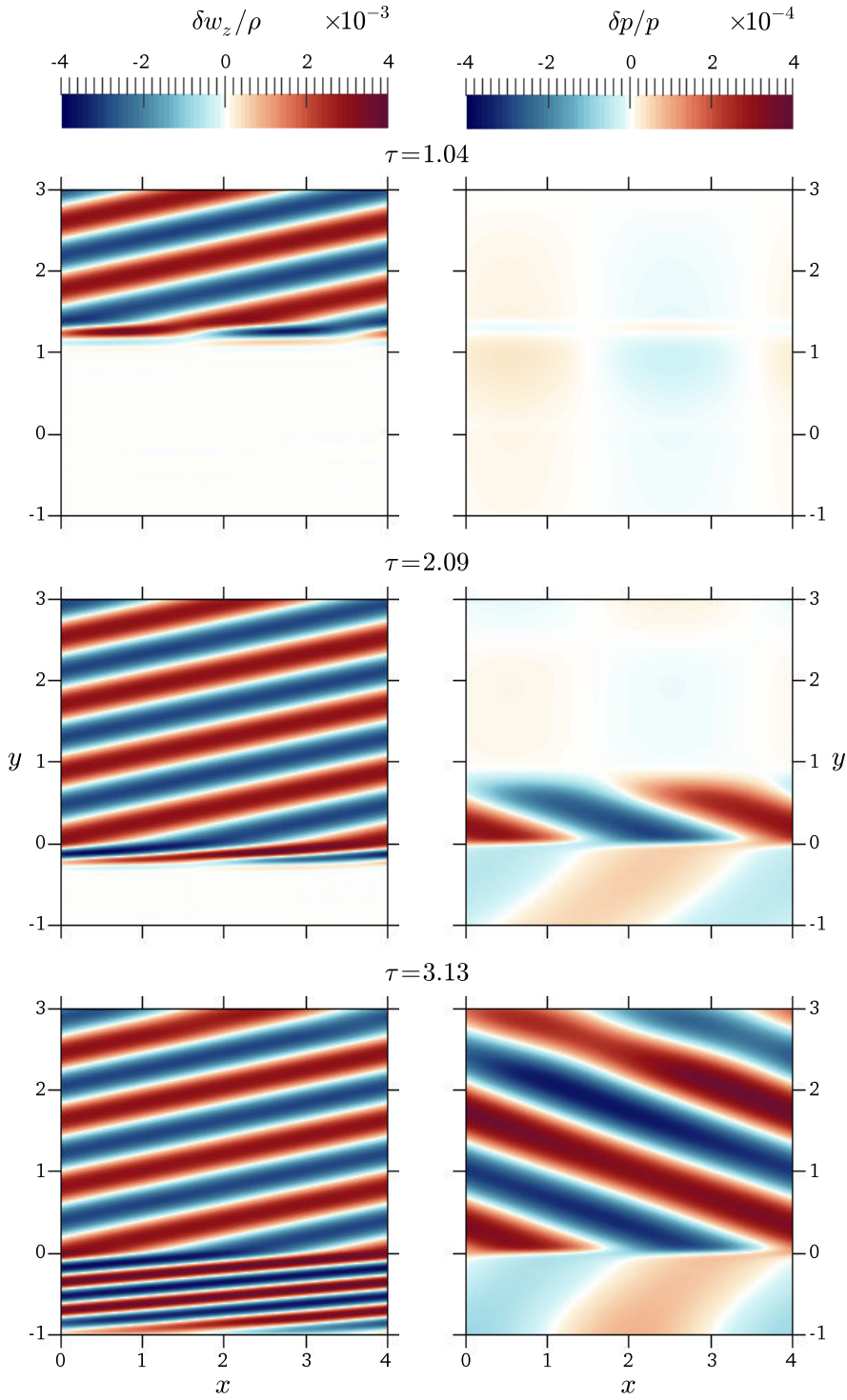
Figure 3.2: Results of sub-problem 1 which can be compared to Fig. 2 in SFF09 [3]. Generation of an acoustic wave by the deceleration of a vorticity wave through a potential step centred at $y_\nabla = 0$ is shown at three successive times τ, normalized by τ_{aac}.

3.2.2 Sub-Problem 2

For the standing shock sub-problem, the results of the well-balanced simulation are shown in Fig. 3.3, here presented to allow easy comparison with Fig. 4 in SFF09. Data is again shown for three successive timepoints, in this instance before and after a pressure wave, injected at the outflow, reaches the shock front. Once there, it produces coupled vorticity/entropy perturbations back into the interior region, with excellent qualitative agreement for the advective-acoustic wave cycling observed with the respective figure in SFF09.

While there are a few very small spurious deviations visible in the specific vorticity (shown in the left hand column of the figure) in the immediate vicinity of the the shock throughout the simulation, the domain is predominantly vorticity-free before the incident wave reaches the shock. Only after the pressure wave, visible in the normalized pressure deviation shown in the right hand column of the figure, impacts the shock is clear generation of advective waves observed. This provides evidence for the necessary second half of the advective-acoustic cycle, complementing the generation of vorticity waves from incident pressure waves at the potential step observed in sub-problem 1.

To once again have a more quantitative check of the results in addition to the qualitative agreement with SFF09 observed above, the amplitude of the resulting entropy wave was measured for comparison to the expected value from theory. This theoretical value can be computed directly according to the formula from SFF09

$$\delta S_{\text{th}} = \frac{\delta p}{p_{\text{in}}} \frac{2}{\mathcal{M}_{\text{in}}} \frac{1 - \mathcal{M}_{\text{in}}^2}{1 + \gamma \mathcal{M}_{\text{in}}^2} \left(1 - \frac{\mathcal{M}_{\text{in}}^2}{\mathcal{M}_1^2} \right) \frac{\mu}{\mu^2 + 2\mu \mathcal{M}_{\text{in}} + \mathcal{M}_1^{-2}}, \qquad (3.21)$$

and for the given simulation is found to be $\delta S_{\text{th}} = 3.28\text{e-}3$.

Analyzing the results of the numerical simulation at the final timetep from the figure, $\tau = 2.47$, the amplitude of the generated entropy wave is measured to be

$$\delta S_{\text{sim}} = 2.94\text{e-}3.$$

This once again demonstrates relatively good agreement between the results obtained using the newly implemented well-balanced method and the theoretically expected value determined from the analytic treatment of F09 and SFF09.

With both parts of the advective-acoustic cycle thus independently observed, it remains to then put the two sub-problems together for a simulation of both effects concurrently.
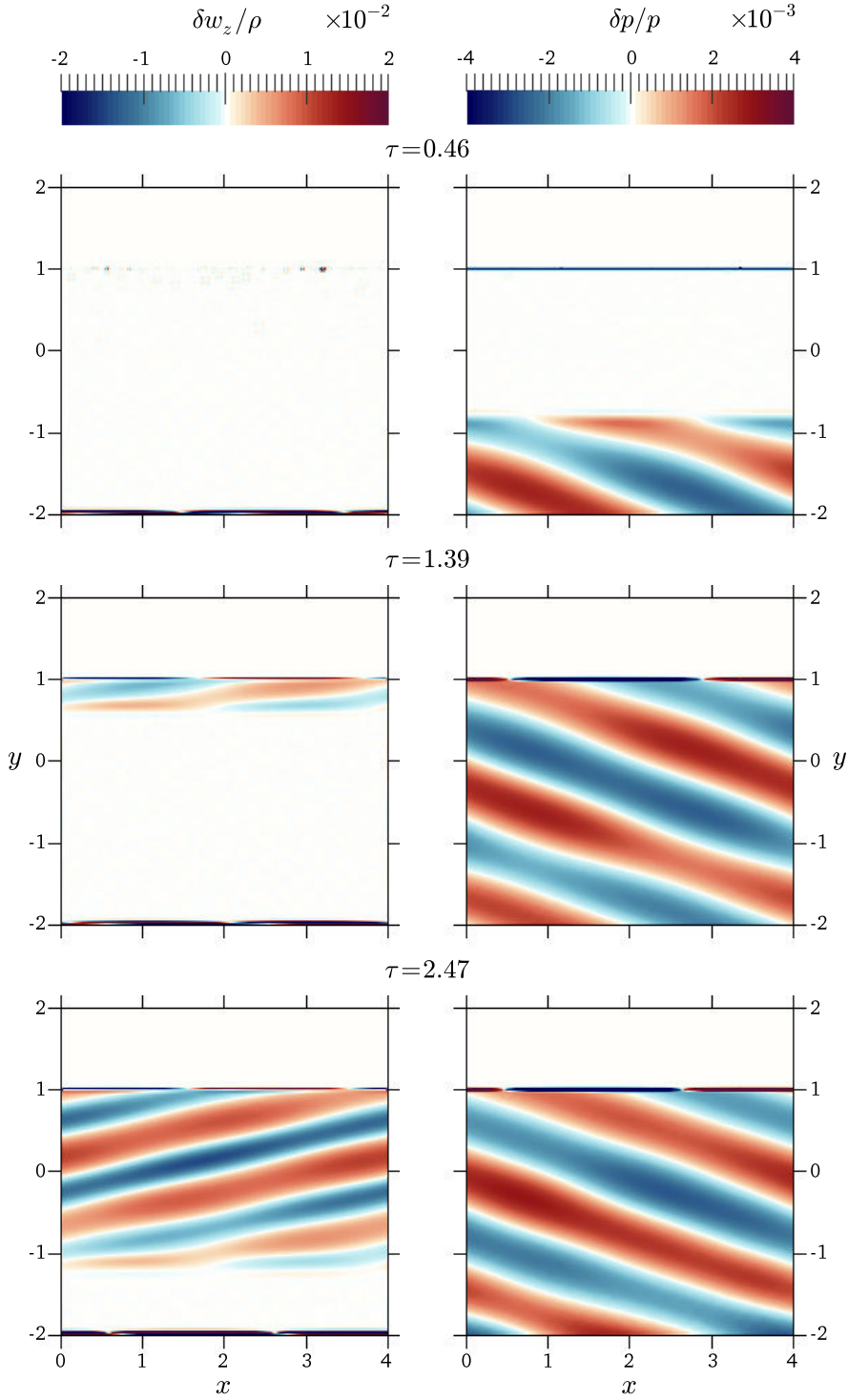
Figure 3.3: Results of sub-problem 2 which can be compared to Fig. 4 in SFF09 [3]. Generation of a vorticity wave by the reflection of an acoustic wave from a shock located at $y_{\mathrm{sh}} = 1$ is shown at three successive times τ, normalized by τ_{aac}.

3.2.3 Full Toy Problem

The complete toy problem was simulated, with both the standing shock and the potential step now present in the domain simultaneously. Perturbations to the density and pressure equilibria were introduced in the supersonic inflow region to mimic spatial inhomogeneities which could be present in the distribution of accreting matter prior to a core-collapse supernova.

Keeping the same horizontal wavenumber $k_x = 2\pi/L_x$ but defining a new vertical wavenumber as $k_y = \omega_0/v_1$ and density perturbation amplitude as $\epsilon_\rho = 10^{-4}$ we have the following equations for the density and pressure perturbations at the supersonic inflow

$$\delta\rho = \epsilon_\rho \cos\left(-\omega_0 t + k_x x + k_y y\right), \tag{3.22}$$

$$p = p_1 + \delta p = (\rho_1 + \delta\rho)RT_1, \tag{3.23}$$

where R is the specific gas constant and the velocity and temperature are kept at constant equilibrium ($\delta v = \delta T = 0$).

Initial conditions were set by splicing together the "settled in" initial conditions used for the shock in sub-problem 2 with the analytically computed equilibrium used for the sub-problem 1 initial conditions, with the join occuring just below the shock at $y = 0.92$. For all quantities Dirichlet boundary conditions were imposed at the inlet with homogenous Neumann conditions used at the outflow.

The simulation was allowed to progress to a final time of $\tau = 3$ (normalized by τ_{aac}) where the time origin $\tau = 0$ was set to be the time just before the incoming perturbations impacted on the shock front. Measurements of the maximal perturbation amplitudes were taken in the interior region between the shock and the potential step, $y \in [0.1, 0.9]$, and these values are tabulated in Table 3.1 for several key timepoints. Visual results for three of these timepoints are also shown in Fig. 3.4 for comparison.

At the first time given in the table, $\tau = 0.125$ (not shown in figure), the incident perturbations have reached the shock and resultant perturbations in both the pressure and vorticity are observed being generated and travelling into the interior region. Neither of these wave types have yet reached the potential step at this point, and so the amplitudes given in the table represent purely the strength of the coupling from the injected perturbations in the supersonic inflow.

Moving to the second time in the table, $\tau = 0.5$ (top row of figure), the faster moving acoustic wave has now reached the potential step, with part of the energy being transmitted through to the outflow and part reflected back into the interior, with the amplitude for the specific pressure perturbation observed to increase noticeably. By contrast, the slower moving advective
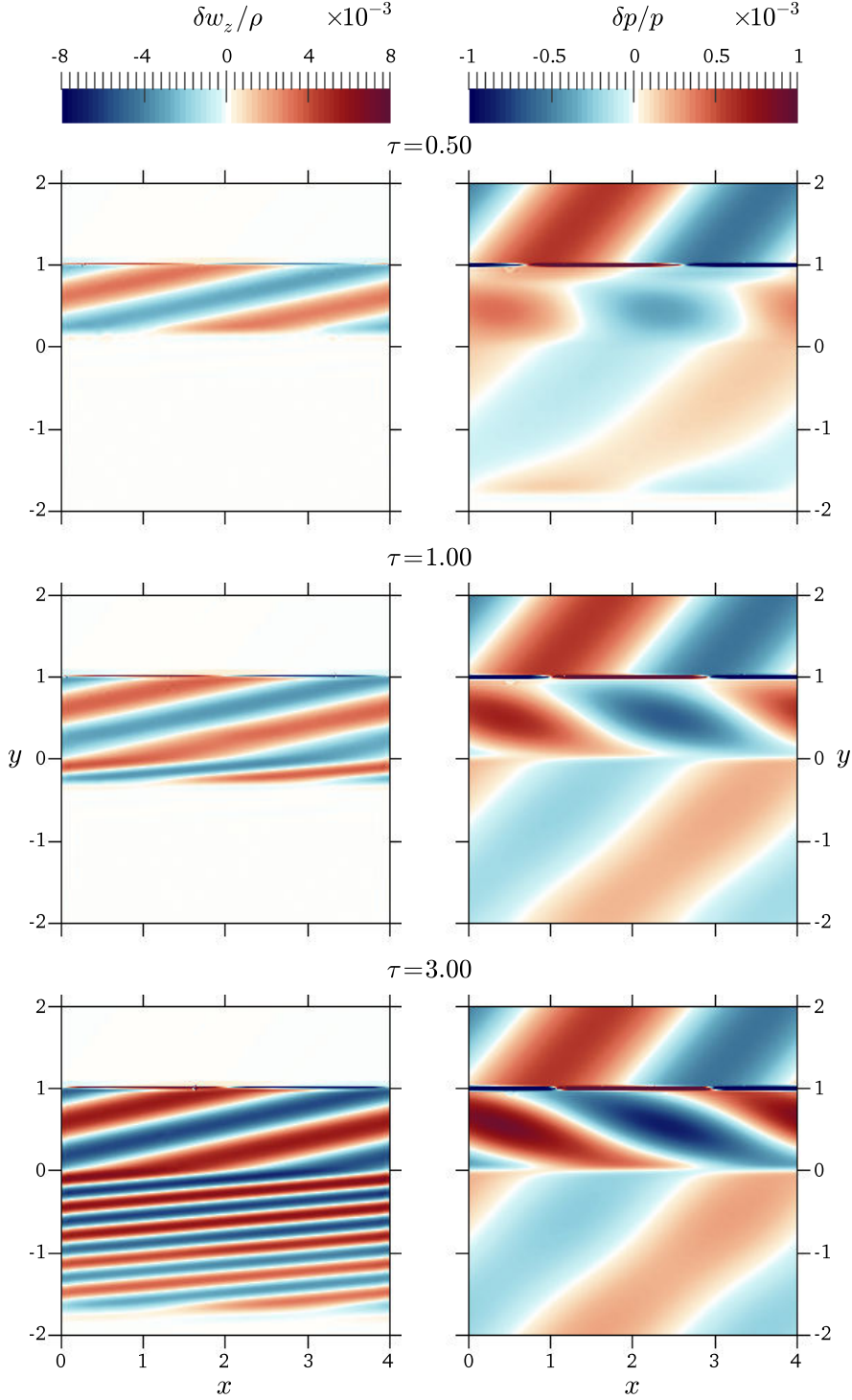
Figure 3.4: Results of the full toy problem simulation, showing the advective-acoustic cycle. Coupling of vorticity and pressure waves at both a shock located at $y_{\mathrm{sh}} = 1$ and a potential step located at $y_{\nabla} = 0$ is shown at three successive times τ, normalized by τ_{aac}.

Table 3.1: Maximum amplitudes of the specific advective and acoustic perturbations in the interior region between the shock and potential step at successive times τ, normalized by τ_{aac}.

	Perturbation Amplitude	
τ	$\delta w_z/\rho$	$\delta p/p$
0.125	2.99e-03	2.83e-04
0.500	3.23e-03	4.01e-04
1.00	3.65e-03	6.65e-04
2.00	5.21e-03	8.12e-04
3.00	5.95e-03	8.89e-04

wave has not yet reached the potential step, and no coupling of acoustic to advective waves is observed at the potential step, and so the measured amplitude of the specific vorticity perturbations has not increased by much from the initial value.

At $\tau = 1$ (middle row of figure), the advective wave has now also reached the potential step, and coupled reflection of acoustic waves back into the interior region is observed, and is evidenced by another significant increase in the measured amplitude of the specific pressure deviation. No reflection of these advective perturbations is observed, of course, but some transmission of vorticity into the outflow can be clearly seen. A small increase in the specific vorticity perturbation amplitude is measured, due to the coupling at the shock of the acoustic reflections from the potential step noted previously at $\tau = 0.5$, but the much larger coupled acoustic waves generated from the advective waves impacting on the potential step have not quite reached the shock at this time.

For the final times represented in the table, $\tau = 2$ (not shown in figure) and $\tau = 3$ (bottom row of figure), the acoustic waves generated by advective coupling at the potential step have now reached the shock and themselves coupled to produce further vorticity perturbations in the interior region, thus completing the full advective-acoustic cycle. This is evidenced by the much more significant increase in the specific vorticity perturbation amplitude compared to the previous time point. Through these final times simulated, the amplitudes for both types of waves continue to rise as further perturbation energy is deposited into the advective-acoustic cycle that is now established between the shock and and the potential step.

Chapter 4

Conclusion

Simulations of physical phenomena involving stationary flows in the presence of external potential fields are encountered in many scientific domains, including weather and climate modelling and astrophysics, and many interesting problems for simulation require accurate resolution of the effects of small perturbations to these equilibria. Within astrophysics, standing accretion shocks (SAS) are a phenomenon of interest, and an instability (SASI) of such spherical shocks has been proposed as a potential component of the evolution of core-collapse supernovae. Since standard shock-capturing finite volume schemes can only resolve the equilibrium state to within the truncation error, it was desirable to develop a scheme to more accurately determine the equilibrium, such that perturbations which are similar to or smaller in scale than the truncation error on realistic meshes can be more efficiently simulated.

Extending on the well-balanced scheme for hydrostatic equilibria developed by Käppeli and Mishra (KM14) [4], a well-balanced scheme for equilibria with non-zero velocity in the presence of an external potential was developed and implemented. The principal component of the new method is a local equilibrium reconstruction scheme used to extend the cell average values of the finite volume scheme to the cell faces. It works by finding a quantity which remains constant under the given thermodynamic constraint for the problem, which for our example derivation was the Bernoulli constant for isentropic flows. Using this constant, the local change in the equilibrium primitive variables can be directly tied to the variation in the external potential, and second-order can be achieved by using a standard limited linear approximation for the deviation of the solution values from this computed local equilibrium. Completion of the well-balancing is then achieved by discretizing the source terms using a suitable differencing of these local equilibrium primitve values.

The method was implemented in the OpenFOAM C++ library, using the

specific assumptions of an ideal gas equation of state and an isentropic flow; however, it is emphasized that the method itself is much more general, and specific implementations could easily be derived for other equations of state or thermodynamic constraints. As well, the current implementation was carried out so as to be suitable for both structured and unstructed grids, a first for this type of well-balanced scheme.

Numerical experiments were conducted to verify the method and implementation, starting with a series of 1D tests on a regular grid using a quintic polynomial external potential function. Simulations of the unperturbed equilibrium confirmed the machine precision accuracy of the new scheme for all grid resolutions compared to the expected first- or second-order truncation error for the unbalanced scheme. Further tests with varying amplitude perturbations on top of this equilibrium flow confirmed the expected convergence for the new scheme, and showed that for small perturbations, significantly coarser meshes could be used with the well-balanced scheme compared to the standard unbalanced scheme to achieve the same level of accuracy, which would make these new schemes much more computationally efficient, particularly as such savings would be compounded in higher dimensional simulations.

The 3D polytrope problem from KM14 was also simulated, here using an unstructured tetrahedral mesh to discretize the spherical domain of interest. Again, machine precision maintenence of the equilibrium flow was observed for the new scheme, confirming both the recovery of the hydrostatic equilibrium of the base method from KM14, as well as the successful extension of the well-balanced method to unstructured meshes, which can be very useful for simulations involving complex geometries not easily meshed using a regular structured grid.

As an application of this new scheme to study the possible underlying causes of the SASI, a simple model problem proposed by Foglizzo (F09) [2] and Sato et al. (SFF09) [3] was simulated. This toy problem consists of a supersonic inflow incident on a stationary planar shock front, followed shortly by a potential step which decelerates the flow, intended to mimic the slowing of incoming matter as it reaches the accreting object. First the two sub-problems were run independently, separating the simulation of the shock and potential step, and the results compared very favourably to those from SFF09 and the analytic treatment of F09. After, the full toy problem was simulated, and showed clear evidence for the advective-acoustic cycle of perturbations in the interior region between the shock and potential step, which has been proposed as a possible driver of the SASI for non-planar shock geometries.

Bibliography

[1] John M. Blondin, Anthony Mezzacappa, and Christine DeMarino. Stability of standing accretion shocks, with an eye toward core-collapse supernovae. *The Astrophysical Journal*, 584(2):971–980, February 2003.

[2] Thierry Foglizzo. A simple toy model of the advective-acoustic instability. I. Perturbative approach. *The Astrophysical Journal*, 694(2):820–832, March 2009.

[3] Jun'ichi Sato, Thierry Foglizzo, and Sébastien Fromang. A simple toy model of the advective-acoustic instability. II. Numerical simulations. *The Astrophysical Journal*, 694(2):833–841, March 2009.

[4] Roger Käppeli and Siddhartha Mishra. Well-balanced schemes for the Euler equations with gravitation. *Journal of Computational Physics*, 259:199–219, February 2014.

[5] Timothy J. Barth and Dennis C. Jespersen. The design and application of upwind schemes on unstructured meshes. In *27th Aerospace sciences meeting*, page 366, January 1989.

[6] Venkat Venkatakrishnan. On the accuracy of limiters and convergence to steady state solutions. In *31st Aerospace Sciences Meeting*, page 880, January 1993.

[7] Venkat Venkatakrishnan. Convergence to steady state solutions of the Euler equations on unstructured grids with limiters. *Journal of Computational Physics*, 118(1):120–130, April 1995.

[8] Krzysztof Michalak and Carl Ollivier-Gooch. Limiters for unstructured higher-order accurate solutions of the Euler equations. In *46th AIAA Aerospace Sciences Meeting and Exhibit*, page 776, January 2008.

[9] Sergei K. Godunov. A difference method for numerical calculation of discontinuous solutions of the equations of hydrodynamics. *Matematicheskii Sbornik*, 47(89):271–306, 1959.

[10] Philip L. Roe. Approximate Riemann solvers, parameter vectors, and difference schemes. *Journal of Computational Physics*, 43:357–372, October 1981.

[11] Viktor V. Rusanov. The calculation of the interaction of non-stationary shock waves and obstacles. *USSR Computational Mathematics and Mathematical Physics*, 1:304–320, March 1961.

[12] Eleuterio F. Toro, Michael Spruce, and William Speares. Restoration of the contact surface in the HLL-Riemann solver. *Shock Waves*, 4:25–34, July 1993.

[13] Marie-Helene Lallemand. *Dissipative Properties of Runge-Kutta Schemes with Upwind Spatial Approximation for the Euler Equations*. PhD thesis, Rapport de Recherche 1179, INRIA Sophia-Antipolis, Valbonne, January 1990.

[14] Chi-Wang Shu and Stanley Osher. Efficient implementation of essentially non-oscillatory shock-capturing schemes. *Journal of Computational Physics*, 77(2):439–471, August 1988.

[15] Colin Barr Macdonald. Constructing high-order Runge-Kutta methods with embedded strong-stability-preserving pairs. Master's thesis, Theses (Dept. of Mathematics), Simon Fraser University, August 2003.

[16] Philip L. Roe. Error estimates for cell-vertex solutions of the compressible Euler equations. *ICASE Report*, (87-6), 1987.

[17] Dana R Lindquist and Michael B Gilest. A comparison of numerical schemes on triangular and quadrilateral meshes. In *11th International Conference on Numerical Methods in Fluid Dynamics*, pages 369–373. Springer, 1989.

[18] Michael B Giles. Accuracy of node-based solutions on irregular meshes. In *11th International Conference on Numerical Methods in Fluid Dynamics*, pages 273–277. Springer, 1989.

ETH

Eidgenössische Technische Hochschule Zürich
Swiss Federal Institute of Technology Zurich

Declaration of originality

The signed declaration of originality is a component of every semester paper, Bachelor's thesis, Master's thesis and any other degree paper undertaken during the course of studies, including the respective electronic versions.

Lecturers may also require a declaration of originality for other written papers compiled for their courses.

_____

I hereby confirm that I am the sole author of the written work here enclosed and that I have compiled it in my own words. Parts excepted are corrections of form and content by the supervisor.

Title of work (in block letters):

WELL-BALANCED METHODS FOR THE COMPUTATION OF THE STANDING ACCRETION SHOCK INSTABILITY (SASI)

Authored by (in block letters):
For papers written by groups the names of all authors are required.

Name(s):	**First name(s):**
MALONEY	SAMUEL

With my signature I confirm that
- I have committed none of the forms of plagiarism described in the 'Citation etiquette' information sheet.
- I have documented all methods, data and processes truthfully.
- I have not manipulated any data.
- I have mentioned all persons who were significant facilitators of the work.

I am aware that the work may be screened electronically for plagiarism.

Place, date	**Signature(s)**
Zürich, January 25, 2019	*Sam Maloney*

For papers written by groups the names of all authors are required. Their signatures collectively guarantee the entire content of the written paper.